Manipulation of mechanically nanopatterned line defect assemblies in plane-parallel nematic liquid crystals

Saša Harkai[1], George Cordoyiannis[1], Adam L. Susser[2], Bryce S. Murray[3], Andrew J. Ferris[2,4], Brigita Rožič[1], Zdravko Kutnjak[1], Charles Rosenblatt[2,*], Samo Kralj[1,5,*]

[1] *Condensed Matter Physics, Jožef Stefan Institute, SI-1000 Ljubljana, Slovenia*

[2] *Department of Physics, Case Western Reserve University Cleveland, Ohio 44106, USA*

[3] *Teledyne Corporation, Thousand Oaks, California 91360 USA*

[4] *Present address: Sandia National Laboratory, Albuquerque, N.M. 87185 USA*

[5] *Department of Physics, Faculty of Natural Sciences and Mathematics, University of Maribor, SI-2000 Maribor, Slovenia*

**The corresponding authors: samo.kralj@um.si, rosenblatt@case.edu*

Abstract

Topological line defects are ubiquitous in nature and appear at all physical scales, including in condensed matter systems, nuclear physics, and cosmology. Particularly useful systems to study line defects are nematic liquid crystals (LCs), where they describe singular or nonsingular frustrations in orientational order and are referred to as disclinations. In nematic LCs, line defects could be relatively simply created, manipulated, and observed. We consider cases where disclinations are stabilized either topologically in plane-parallel confinements or by chirality. In the former case, we report on studies in which defect core transformations are investigated, the intriguing dynamics of ½ strength disclinations in LCs exhibiting negative dielectric anisotropy, and stabilization and manipulation of assemblies of defects. For the case of chiral nematics, we consider nanoparticle-driven stabilization of defect lattices. The resulting line defect assemblies could pave the way to several applications in photonics, sensitive

detectors, information storage devices. These excitations, moreover, have numerous analogs in other branches of physics. Studying their universal properties in nematics could deepen understanding of several phenomena, which are still unresolved at the fundamental level.

1.Introduction

Topological defects [1] (TDs) refer to topologically stabilized localized distortions in a physical field describing the ordering of a system. They appear in phase transitions in which the symmetry of the system is reduced. The sole condition for their appearance is symmetry breaking and causality [2,3] (i.e. finite speed of information propagation). Consequently, they are present at all physical scales [3], and thus are important in particle physics, condensed matter physics, and cosmology.

In general, the ordering of a symmetry broken phase is described in terms of order parameter fields, which consist of two qualitatively different contributions [4]: *amplitudes* and *phases*. *Amplitudes* reflect the magnitude of the established order and are, in general, single-valued for a given set of control parameters such as temperature. *Phases* determine symmetry breaking "selection" among a degenerate set of possible states, which is infinite for continuous symmetry breaking transitions. (Note that in this case "continuous" does not refer to a second order phase transition, but rather to the *phase*-field degeneracy in the symmetry broken phase). Frustrations in the *phase*-field could lead to topological defects, which appear either as point-like, line-like, and wall-like configurations. Their topological stability could be determined using the group theory considerations [1,5].

Owing to their topological origin, the behaviour of TDs exhibits a rich variety of

universalities that are independent of the systems' microscopic details. Consequently, it is advantageous to find systems in which TDs can be created, manipulated, and observed with relative ease. For this purpose, various liquid crystalline (LC) phases [4,6,7] satisfy these requirements and, importantly, they exhibit many diverse types of TDs [4,8,9]. Furthermore, the unique combination of liquid-like behavior, softness (i.e. strong stimuli responsivity), and optical anisotropy enables experimentally efficient manipulation and observations of TDs.

Thermotropic uniaxial nematic phases represent the simplest LC configurations exhibiting only orientational long-range order, which is commonly described by the tensor nematic order parameter $\boldsymbol{Q}$ [4,6]. The latter is, at the lowest approximation, described by the uniaxial nematic order parameter S and the nematic director field $\hat{\boldsymbol{n}}$, representing the amplitude and phase order parameter components, respectively. Nematic phase order is formed via an order-disorder symmetry-breaking phase transition on cooling from the isotropic phase. Topological arguments [5,8] reveal that either point or line-defects could be topologically protected in the nematic phase.

We note that the resulting bulk equilibrium phases are defectless in achiral and weakly chiral LCs, see Figure 1(a) and Figure 1(b). These configurations are referred to as the nematic (N) and cholesteric (N^*) phase [4,6], respectively. In both phases $S(\boldsymbol{r})$ is spatially homogeneous. Furthermore, in the N phase $\hat{\boldsymbol{n}}(\boldsymbol{r})$ is aligned spatially homogeneously along a single symmetry direction. On the other hand, the director pattern in N^* consists of a continuous rotation of the nematic director $\hat{\boldsymbol{n}}(\boldsymbol{r})$, which twists along the symmetry breaking helical axis perpendicular to the director. Relatively strongly chiral LCs can exhibit the so-called blue phases (BPs) [9,10], which are characterized by lattices of disclinations (see Figure 1(c-e)). Three qualitatively

different configurations have been reported, referred to as BPI (Figure 1(c)), BPII (Figure 1(d)), and BPIII (Figure 1(e)). These structures are fingerprinted by body-centered cubic, simple cubic, and glass-like lattices of disclinations, respectively.

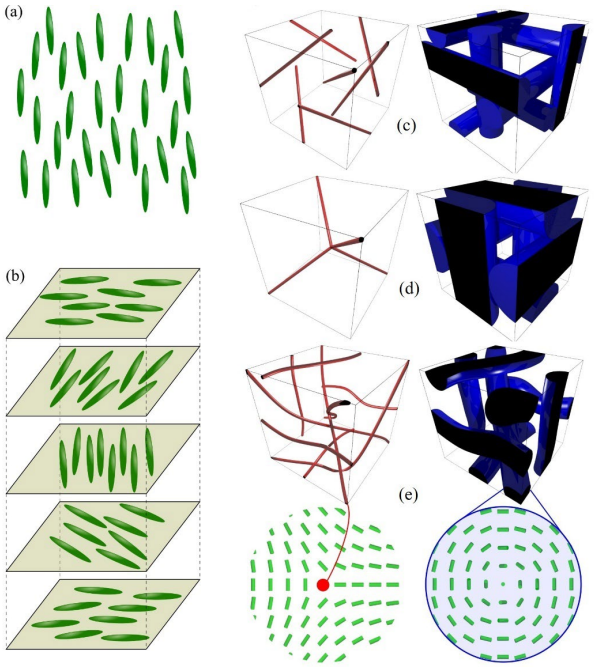

Figure 1. Schematic presentation of the (a) nematic, b) cholesteric, c) BPI, d) BPII, e) BPIII liquid crystalline configurations.

Nematic LCs represent a superb experimentally accessible playground in which to study the physics of topological defects [5]. Moreover, diverse defect patterns in LCs could be exploited in various applications such as in photonics, sensitive detectors, displays, and photovoltaics [11-16]. In particular, TDs in LCs can be exploited as efficient traps of appropriate nanoparticles [17-20] or colloids [21-23], which enormously increases the potential use of TDs in future applications.

In this article we examine diverse disclination patterns in nonchiral and chiral nematic LCs confined within three-dimensional plane-parallel cells. To be sure, this is a vast area of research, and we have chosen to focus most heavily on work from our

groups. Nevertheless, there are several recent review articles that focus on related, but distinctly different areas. These include reviews on quasi 2D geometries by Harth and Stannarius [24], in which the focus is on free standing smectic films, especially in the smectic-C phase. Shin and Yoon [25] examined various techniques, both surface and external fields, to manufacture and manipulate defects. Ultimately their goal was to explore various applications of defects, including particle manipulation, switchable electrooptics, and lenses. A group from IIT Gandhinagar [26] examined the well-developed field of colloids in nematic liquid crystals [27,28], their resulting defects and ultimately their manipulation and dynamic behaviour. Research in active nematic liquid crystals [29], which consist of self-propulsion of high density anisometrically-shaped objects, such as biopolymers and bacteria, has been growing rapidly. The spontaneous generation (or destruction) of topological defects often ensues from the resulting motion. Work on motile topological defects in 2D systems, and more recently on 3D, is reviewed by Doostmohammadi et al. [30], where they compared the active systems with disclination lines and closed loops generally found in passive liquid crystal systems. They noted that because most work on active nematics has focused on 2D systems, it is poorly understood how active turbulence affects the disclination lines in 3D.

Here we focus on the more traditional passive systems and illustrate reversible external electric field-driven transformations among competing structures. Additionally, we demonstrate the impact of different nanoparticles (NPs) on BP configurations. Our plan is as follows. In Sec. 2 we present a Landau-de Gennes phenomenological model and discuss nematic excitations. In Sec. 3 we present the basic mechanisms that enable the creation and stabilization of TDs in simple plane-parallel confinements. In Sec. 4 stabilization and external electric field manipulation of diverse line defect patterns in nonchiral nematics are reported, with emphasis on mechanical nanopatterning to

implement the desired defects. Sec. 5 is devoted to the impact of different NPs on the stability of BPs in chiral nematics. In the final section, we summarize findings.

2. Mesoscopic modelling

We first introduce mesoscopic modelling, which is commonly used to describe core structure and assemblies of disclinations in nematic LCs. Key quantities describing topological properties of disclinations are introduced, as well as the excitations that could nucleate the defects.

2.1. Order parameter

One commonly describes nematic order in terms of the traceless symmetric tensor order parameter [4,6]

$$\boldsymbol{Q} = \sum_{i=}^{3} \lambda_i \hat{\boldsymbol{e}}_i \otimes \hat{\boldsymbol{e}}_i, \tag{1}$$

where λ_i and $\hat{\boldsymbol{e}}_i$ stand for eigenvalues and eigenvectors of $\boldsymbol{Q}$, respectively. This parametrization encompasses both uniaxial and biaxial states. In nematic uniaxial LCs the former states exist in the presence of sufficiently strong local distortions. Uniaxial states are expressed by

$$\boldsymbol{Q} = S(\hat{\boldsymbol{n}} \otimes \hat{\boldsymbol{n}} - I/3)\,, \tag{2}$$

where $S \in [-0.5,1]$ stands for the nematic uniaxial order parameter. Note that states with $S > 0$ ($S < 0$) are at the mesoscopic level and are commonly geometrically portrayed by prolate (oblate) cylindrically symmetric objects. Disordered (isotropic) states correspond to $S = 0$.

A convenient parametrization emphasizing biaxial order is [31]

$$\lambda_1 = \frac{2}{3}\lambda_0 \cos(\gamma),\ \lambda_2 = -\frac{2}{3}\lambda_0 \cos(\gamma - \pi/3),\ \lambda_3 = -\frac{2}{3}\lambda_0 \cos(\gamma + \pi/3), \tag{3a}$$

$$\lambda_0 = \sqrt{\frac{3}{2} Tr \boldsymbol{Q}^2}. \tag{3b}$$

This parametrization describes the amplitude order parameter space $\{\lambda, \gamma\}$ for a fixed orientation of the eigenvectors $\{\hat{\boldsymbol{e}}_1, \hat{\boldsymbol{e}}_2, \hat{\boldsymbol{e}}_3\}$, see Figure 2. Furthermore, the degree of biaxiality is measured by the biaxial parameter [31,32]

$$\beta^2 = 1 - \frac{6(Tr\boldsymbol{Q}^3)^2}{(Tr\boldsymbol{Q}^2)^3} = sin^2(3\,\gamma) \in [0,1], \tag{4}$$

where $\beta^2 = 0$ and $\beta^2 > 0$ reflect uniaxial and biaxial states. In particular, the condition $\beta^2 = 1$ corresponds to states exhibiting maximal biaxiality.

The Isotropic phase is represented by $\lambda_0 = 0$. Positive uniaxial states (i.e. S>0) for ordering along $\{\hat{\boldsymbol{e}}_1, \hat{\boldsymbol{e}}_2, \hat{\boldsymbol{e}}_3\}$ are determined by $\{\gamma = 0, \gamma = \frac{2\pi}{3}, \gamma = -2\pi/3\}$, and negative uniaxial states (i.e. S<0) by $\{\gamma = \pi, \gamma = -\frac{\pi}{3}, \gamma = \frac{\pi}{3}\}$. The remaining values of γ describe biaxial states. In particular, the states $\{\gamma = \pm\frac{\pi}{6}, \gamma = \pm\frac{\pi}{2}, = \pm\frac{5\pi}{6}\}$ correspond to configurations exhibiting maximal biaxiality.

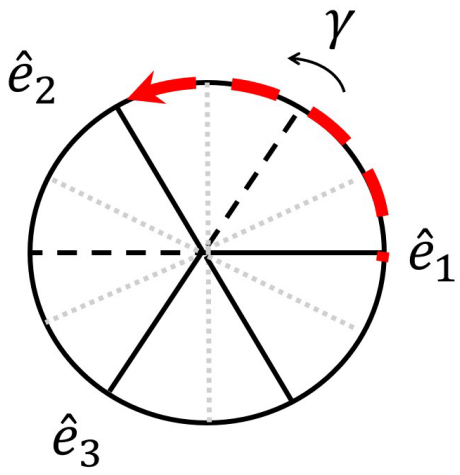

Figure 2. *Amplitude* order parameter space $\{\lambda_0, \gamma\}$ of the nematic tensor order parameter, where λ_0 is the radius and γ as the angle. The $\boldsymbol{Q}$ eigenframe is determined by $\{\hat{\boldsymbol{e}}_1, \hat{\boldsymbol{e}}_2, \hat{\boldsymbol{e}}_3\}$. The center and the outer radius of the circle correspond the isotropic phase and $\lambda_0 = S_{eq}$, where S_{eq} minimizes the condensation free energy penalty. The

states $\{\gamma = 0, \gamma = \frac{2\pi}{3}, \gamma = -2\pi/3\}$ describe positive uniaxial order along $\{\hat{\boldsymbol{e}}_1, \hat{\boldsymbol{e}}_2, \hat{\boldsymbol{e}}_3\}$. The path indicated by the dashed red color indicates order reconstruction transformation, where the nematic order reconfigures from $\hat{\boldsymbol{n}} = \hat{\boldsymbol{e}}_1$ to $\hat{\boldsymbol{n}} = \hat{\boldsymbol{e}}_2$ via intermediate biaxial states and a negative uniaxial state along $\hat{\boldsymbol{e}}_2$ (at $\gamma = \pi/3$). Note that this transformation does not require melting of the nematic order. In the case shown, the amplitude of nematic order is constant. Such cases could be realised deep in the nematic phase.

2.2. Free energy

Within the Landau-de Gennes mesoscopic approach, the LC free energy is traditionally expressed as [4,6]

$$F = \int f dV + \int f_i dA \,, \tag{5}$$

where the first integral is carried over the LC body and the second over the LC-confining interface. We write the bulk free energy density $f = f_h + f_e + f_f$ as the sum of homogeneous (f_h), elastic (f_e), and external electric $\boldsymbol{E}$ and magnetic $\boldsymbol{H}$ field (f_f) contributions, and f_i determines interactions at the LC-limiting interface. These contributions are expanded in terms of the nematic order parameter. In the expansion we use the minimal set of symmetry allowed terms that are needed to describe phenomena presented in this review [4,6,33,34]:

$$f_h = \frac{3}{2}a_0(T - T^*)Q_{\alpha\beta}Q_{\alpha\beta} - \frac{9}{2}bQ_{\alpha\beta}Q_{\beta\gamma}Q_{\gamma\alpha} + \frac{9}{4}c\left(Q_{\alpha\beta}Q_{\alpha\beta}\right)^2, \tag{6a}$$

$$f_e = \frac{L_1^{(1)}}{2}Q_{\alpha\beta,\alpha\beta} + \frac{L_1^{(2)}}{2}Q_{\alpha\beta,\gamma}Q_{\alpha\beta,\gamma} + \frac{L_2^{(2)}}{2}Q_{\alpha\beta,\beta}Q_{\alpha\gamma,\gamma} + \frac{L_3^{(2)}}{2}Q_{\alpha\beta,\gamma}Q_{\beta\gamma,\alpha} + 2L_{ch}q_{ch}\varepsilon_{\alpha\beta\gamma}Q_{\alpha\beta}Q_{\alpha\beta,\gamma}, \tag{6b}$$

$$f_f = -\frac{\varepsilon_0\Delta\varepsilon}{2}E_\alpha Q_{\alpha\beta}E_\beta - \frac{\mu_0\Delta\mu}{2}H_\alpha Q_{\alpha\beta}H_\beta, \tag{6c}$$

$$f_i = \frac{w}{2}\left(Q_{\alpha\beta} - Q_{\alpha\beta}^{(i)}\right)\left(Q_{\alpha\beta} - Q_{\alpha\beta}^{(i)}\right). \tag{6d}$$

In this notation the numerical coefficients are introduce for later convenience, the summation over the repeated indices is applied, $(\dots)_{,\gamma} = \frac{\partial(\dots)}{\partial x_\gamma}$ denotes the partial derivative with respect to the Cartesian coordinate x_γ, and $\varepsilon_{\alpha\beta\gamma}$ is the Levi-Cevita antisymmetric tensor [35]. The remaining quantities are described below.

The homogeneous term (Eq.(6a)) is expressed up to the fourth term in $\boldsymbol{Q}$, which is needed to describe the bulk spontaneous temperature driven discontinuous phase transition in orientational order at $T = T_{IN}$, and it enforces uniaxial nematic order below T_{IN}. Here a_0, *b, c* represent positive temperature independent Landau phenomenological coefficients, and T^* is the bulk isotropic phase supercooling temperature. The value of bulk equilibrium (spatially homogeneous) uniaxial nematic order S_{eq} in the absence of external fields is given by

$$S_{eq}(T \le T_{IN}) = S_0 \frac{3+\sqrt{9-\frac{8(T-T^*)}{T_{IN}-T^*}}}{4},\ S_{eq}(T > T_{IN}) = 0, \tag{7}$$

where $T_{IN} = T^* + \frac{b^2}{4a_0 c}$, and $S_0 = S_{eq}(T = T_{IN}) = \frac{b}{2c}$.

In Eq.(6b) we present symmetry allowed elastic contributions up to the quadratic $\boldsymbol{Q}$ expansion. These terms penalize departures from a spatially homogeneous order. The symmetry allowed invariants are weighted by the bare (temperature independent) nematic elastic constant $L_1^{(1)}$, $L_1^{(2)}$, $L_2^{(2)}$, $L_3^{(2)}$, L_{ch} [4,33]; additionally, q_{ch} represents the LC inherently preferred chirality wave vector. In the case of nematic uniaxial order (see Eq.(2)), which is favored by f_h, the elastic term is commonly expressed as

$$f_e = \frac{K_{11}}{2}(\nabla \cdot \hat{\boldsymbol{n}})^2 + \frac{K_{22}}{2}(\hat{\boldsymbol{n}}.\nabla \times \hat{\boldsymbol{n}} - q_{ch})^2 + \frac{K_{33}}{2}|\hat{\boldsymbol{n}} \times \nabla \times \hat{\boldsymbol{n}}|^2 - K_{24}\nabla \cdot (\hat{\boldsymbol{n}}\nabla \cdot \hat{\boldsymbol{n}} + \hat{\boldsymbol{n}} \times \nabla \times \hat{\boldsymbol{n}}), \tag{8}$$

This is the so called Oseen-Frank free energy [6,36], expressed in terms of the temperature dependent splay (K_{11}), twist (K_{22}), bend (K_{33}), and saddle-splay (K_{24}) Frank

elastic constants. This expression is commonly used if one describes nematic order solely by $\hat{\boldsymbol{n}}$. The temperature dependence of these constants is obtained by inserting the uniaxial order parameter given by Eq.(2) into Eq.(6b) and collecting the contributions that weight splay, twist, bend, and saddle-splay nematic distortions. Note that in earlier studies the saddle-splay contribution was commonly neglected because its contribution can be transformed to the interface enclosing the nematic body. However, it later emerged that this constant could strongly affect stability and structure of TDs. Frequently the single nematic elastic constant approximation is used. In using a representation in terms of bare nematic constants, one commonly imposes $L \equiv L_1^{(2)} = L_{ch}$, and the remaining constants are set to zero. Furthermore, using Frank constants, one commonly imposes $K \equiv K_{11} = K_{22} = K_{33} = K_{24}$.

The quantities in the external field free energy contribution in Eq.(6c) refer to the vacuum electric permittivity ε_0 and the vacuum magnetic permittivity μ_0. The quantity $\Delta\varepsilon$ stands for the dielectric anisotropic response in an external electric field $\boldsymbol{E}$, and $\Delta\mu$ quantifies the magnetic anisotropic response in an external magnetic field $\boldsymbol{H}$. For positive anisotropies (i.e., $\Delta\varepsilon > 0, \Delta\mu > 0$) and negative anisotropies, the uniaxial LC molecules tend to align $\hat{\boldsymbol{n}}$ parallel and perpendicular to relevant external field, respectively.

We model the conditions at the confining substrate using Eq.(6d) [34,37]. It is weighted by the positive constant *w*, which tends to enforce the nematic order $\boldsymbol{Q}_i$ that is locally imposed by the interface. This term was originally introduced by Nobili and Durand [34] and exhibits the classical Rapini Papoular form [37] by setting $\boldsymbol{Q_i} = S_i\left(\hat{\boldsymbol{n}}_i \otimes \hat{\boldsymbol{n}}_i - \frac{I}{3}\right)$. In this case the interactions tend to align the nematic director along the easy axis $\hat{\boldsymbol{n}}_i$ and enforces the amplitude S_i.

In this contribution we will mostly use a single elastic constant (using L or $K{\sim}LS^2$) approximation to illustrate the key features of interest. Furthermore, we will confine our attention to responses to an external electric field.

The model introduces several characteristic length scales [4,6] that determine order of magnitude responses of the LC to different perturbations. For later convenience we introduce the uniaxial coherence length ξ, biaxial coherence length ξ_b, external electric field extrapolation length ξ_E, and surface extrapolation length d_e. In the nematic phase we define these quantitites as [4,31]

$$\xi = \sqrt{L/\frac{\partial^2 f_h^{(eq)}}{\partial S^2}},\ \xi_b = \sqrt{L/(bS_{eq})},\ \xi_E = \sqrt{LS_{eq}/(\varepsilon_0 \Delta\varepsilon E^2)}, \tag{9}$$

where the second derivative $\frac{\partial^2 f_h^{(eq)}}{\partial S^2}$ is expressed for $S = S_{eq}$.

2.3. Excitations

2.3.1. Fundamental excitations

We first consider fundamental excitation modes in nematic order. In particular, we focus on those that could nucleate stable arrays of disclinations. One gains insight into the representative fundamental excitations in nematic order by focusing on uniaxial elastic free energy penalties in the equal elastic constant approximation. These are determined by $\nabla\hat{\boldsymbol{n}} = \partial_i n_j$, which can be decomposed into four fundamental modes [38-40], referred to as the *bend* (*B*), *splay* (*SP*), *twist* (*T*), and *tetrahedral splay* (Δ) mode:

$$\partial_i n_j = -n_i B_j + \frac{SP}{2}(\delta_{ij} - n_i n_j) + \frac{T}{2}\epsilon_{ijk} n_k + \Delta_{ij}. \tag{10}$$

These excitations correspond to four irreducible representations of the group of rotations about $\hat{\boldsymbol{n}}$ [38]. They could be locally excited individually while the other modes are absent. The first three modes are defined as [39], as $B = \hat{\boldsymbol{n}} \times \nabla \times \hat{\boldsymbol{n}}$, $SP = \nabla \cdot \hat{\boldsymbol{n}}$, and $T = \hat{\boldsymbol{n}} \cdot \nabla \times \hat{\boldsymbol{n}}$. The *bend* mode *B* corresponds to a "pure" (i.e. other distortions are absent) bend elastic distortion (see Figure 3(a)). The *splay* mode *SP* corresponds to

isotropic inward or outward (see Figure 3(b)) tilt deformation in the plane perpendicular to $\hat{\boldsymbol{n}}$. The *twist* mode T exhibits a right-handed or left-handed (see Figure 3(c)) twist isotropically in the plane perpendicular to $\hat{\boldsymbol{n}}$. Note that only the *bend* mode is equal to the *classical bend* deformation introduced in Oseen-Frank approach [36]. The remaining two (i.e. *splay* and *twist* modes) exhibit isotropic distortions, dubbed double-splay and double-twist, respectively. On the contrary, their more familiar Oseen-Frank modes, *classical splay* and *classical twist*, distortions exhibit single (i.e. planar) splay and twist deformation, respectively. The remaining *splay tetrahedral* mode is defined by $\Delta_{ij}= \partial_i n_j + n_i B_j - \frac{SP}{2}(\delta_{ij} - n_i n_j) - \frac{T}{2}\epsilon_{ijk} n_k$. This deformation has the symmetry of a tetrahedron (see Figure 3(d)). In this model $\hat{\boldsymbol{n}}$ tips outwards along one axis and inward along the other axis.

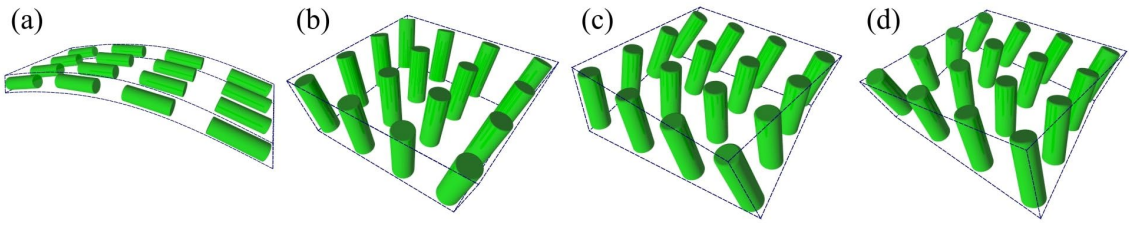

Figure 3. Fundamental excitations in orientational order: (a) bend, (b) splay, (c) twist, and (d) Δ mode.

Note that the classical Oseen-Frank free energy density is given by [6,36]

$$f = \frac{K_{11}}{2} SP^2 + \frac{K_{22}}{2} T^2 + \frac{K_{33}}{2} |B|^2 - K_{24} \nabla \cdot (\hat{\boldsymbol{n}} \nabla \cdot \hat{\boldsymbol{n}} + \hat{\boldsymbol{n}} \times \nabla \times \hat{\boldsymbol{n}}). \quad (11)$$

Note that classical single splay, single twist, bend, and saddle-splay excitations are not independent. On the contrary, fundamental modes could be selectively excited. In terms of the Oseen-Frank free energy density they can be expressed as [39]

$$f = \frac{K_{11}-K_{24}}{2} SP^2 + \frac{K_{22}-K_{24}}{2} T^2 + \frac{K_{33}}{2} |B|^2 + K_{24} \mathrm{Tr}\Delta^2. \quad (12)$$

It follows that elastic deformations corresponding to pure double-splay ($K_{11}^{(DS)}$), double-twist ($K_{22}^{(DT)}$), bend, and tetrahedral splay are weighted by elastic constants $K_{11}^{(DS)} = K_{11} - K_{24}$, $K_{22}^{(DT)} = K_{22} - K_{24}$, K_{33}, and K_{24}. The system is positive definite if these constants are positive, which in fact embodies the Ericksen stability condition [41]. Note that double-twist and tetrahedral splay excitations cannot fill the entire 3D Euclidian space and the resulting frustration is resolved by introducing TDs.

2.3.2. Topological defects and topological invariants

Next, we consider topologically stable localized excitations, corresponding to topological defects. To gain insight into their key structural and topological properties we consider again the simplest nematic Oseen-Frank [6,36] uniaxial description in terms of $\hat{\boldsymbol{n}}$. In the 2D xy-plane and in the approximation of equal Frank elastic constants, the Euler-Lagrange equation is $\nabla^2 \psi = 0$. Here we use the parametrization $\hat{\boldsymbol{n}} = \hat{\boldsymbol{e}}_x cos\psi + \hat{\boldsymbol{e}}_y sin\psi$. The equation's solution is

$$\psi = s\varphi + \psi_0, \tag{13}$$

where $\varphi = ArcTan(y/x)$, ψ_0 is a constant, and s is the so-called "winding number" (or Frank index). Configurations determined by $s=0$ correspond to equilibrium nematic configurations (i.e. ground states), where ψ_0 defines a symmetry breaking direction. Structures with $s\neq 0$ describe singular solutions, where s is a discrete topological invariant possessing either half integer or full integer values. In 2D s is equivalent to the topological charge, which is a conserved quantity. Note that half integer values reflect the nematic head-to-tail invariance. Different defect structures described by Eq.(13), where the defect center is at the coordinate origin, are plotted in Figure 4. TDs with $s>0$ and $s<0$ are commonly referred as *defects* and *antidefects*, respectively. A {*defect,antidect*} pair,

bearing opposite signs of *s*, tends to annihilate into a defectless state, because the defects are in general energetically costly.

The general solution that describes assembly of *N* noninteracting defects is given by

$$\psi = \sum_{i=1}^{N} s_i ArcTan\left(\frac{y-y_i}{x-x_i}\right) + \psi_0 \,, \tag{14}$$

where s_i determines the winding number of the i[th] defect whose origin is placed at (x_i, y_i).

In 3D the defect structures presented in Figure 4 correspond either to point or line defects. In this case Figure 4(a,b,c,f) describe line defects that are running out of the page. Furthermore, Figure 4(d,e) could represent either point defects or line defects. Note that in Figure 4 the structure of defects is presented in the uniaxial approximation, where the orientational field characterizing defects is given by $\hat{\boldsymbol{n}}$.

In this review we focus on line defects, which form either closed loops or originate and terminate at a surface that is in contact with a LC body. These structures are commonly described by the winding number *s* (which reflects local line defect structure), and by the 3D topological charge *q*, which is a whole integer [8].

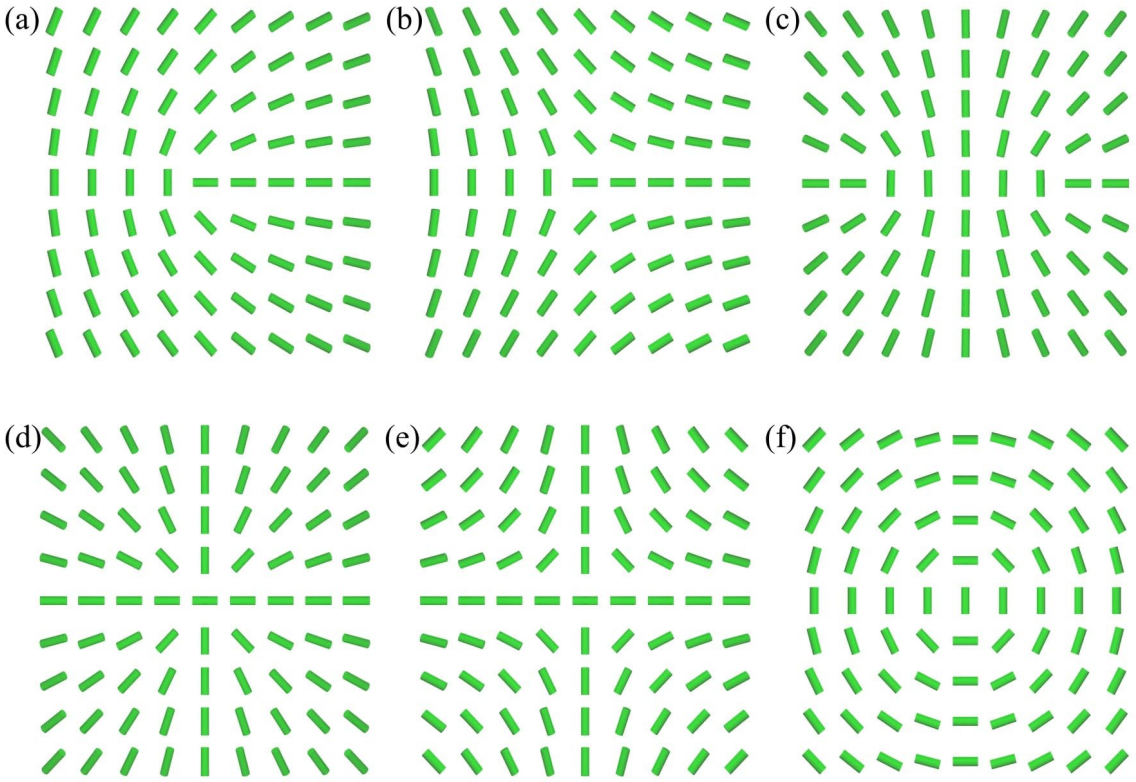

Figure 4. 2D schematic representations of some typical surface topological defects described by Eq. (11). (a) s=1/2, $\psi_0 = 0$; (b) s=-1/2, $\psi_0 = 0$; (c) a pair of s=1/2 defects; (d) s=1, $\psi_0 = 0$; (e) s=-1, $\psi_0 = 0$; (f) s=1, $\psi_0 = \pi/2$.

The core structure of TDs is, in general, biaxial, and therefore requires a description in terms of tensor order parameter. For example, point defects in 3D could exhibit either uniaxial or biaxial structure. In the former case, where a cross-section of a representative spherically symmetric hedgehog structure is shown in Figure 4(d), the center of the defect is melted, and the linear core size is determined by the uniaxial correlation length ξ [42]. This uniaxial spherically symmetric structure is generally unstable (or metastable) with respect to the biaxial and cylindrically symmetric structure [43,44]. The latter is characterized by a ring exhibiting negative uniaxiality, which is embedded in a torus exhibiting maximal biaxiality. Furthermore, the defect symmetry axis is positively uniaxial, and the far field of an isolated defect is radial and positive uniaxial. Frustrations

in orientational order within the defect core may be realized *via* an order reconstruction mechanism (i.e. exchange of $\boldsymbol{Q}$ eigenvalues). Consequently, key structural changes within the defect core could be described by variations in the amplitude order parameter space (i.e. the variables λ_0 and γ in Eqs.(3)). The characteristic linear size of a biaxial point defect is well estimated by the biaxial coherence length ξ_b [44,45].

The characteristic loop of a biaxial hedgehog corresponds, in fact, to an s=1/2 line defect if the loop length is increased. This could be achieved, for example, by applying a sufficiently strong electric field to a LC possessing positive dielectric anisotropy. Furthermore, an antihedgehog (i.e. the antidefect companion of the hedgehog structure) is characterized by a loop [44,46–48], whose enlarged structure corresponds to the line defect of strength s=-1/2. In general, line defects form either closed loops or originate and terminate at a substrate that is in contact with a LC. The line structures described above are "charged" in the sense that they can be assigned a 3D topological charge q=1, *i.e.* their far field nematic structure is spatially distorted. These extended structures are shown in Figure 5(a,b), where they are stabilized by an appropriate confining surface treatment, as will be described in detail in the following sections. Furthermore, a line defect characterized locally by $|s| = 1/2$ could be chargeless if the sign of s changes along the defect line. An example of such a defect is shown in Figure 5(c). Such a defect is characterized by q=0, and consequently its far field nematic structure could be undistorted (spatially homogeneous). Note that all line defects in 3D are characterized by $|s| = 1/2$ and are topologically equivalent. The core structure of these defects is always biaxial [43,49]. At the defect center line these defects are negatively uniaxial and are embedded in a sheet exhibiting maximal biaxiality [44].

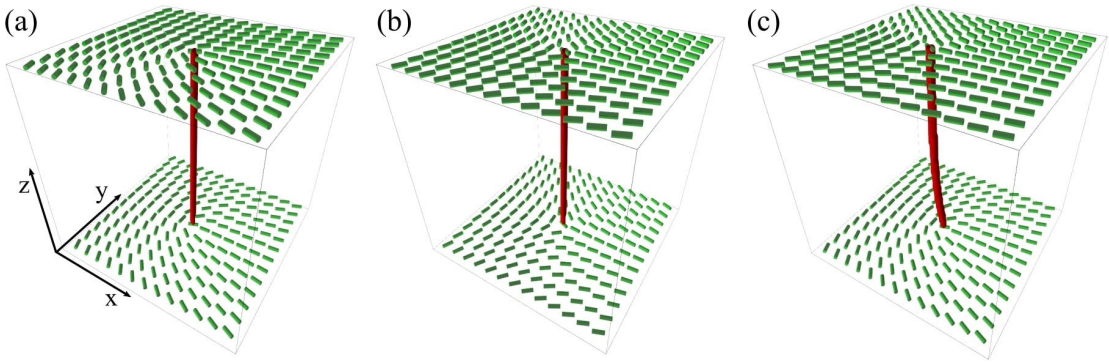

Figure 5. Charged (a,b) and chargeless line defects (c). (a) s=1/2, $|q|$=1; (b) s=-1/2, $|q|$=1; $|s|$=1/2, q=0.

3. Creation and stabilization of TDs

In general TDs are energetically expensive. If the total 3D topological charge of a LC body equals zero, then the system rarely exhibits steady state TDs, unless they are pinned by a surface imperfection or dust. Nevertheless, they are relatively ubiquitous at – least temporarily – when the ordered phase is condensed via a sufficiently rapid phase transition. In static configurations, TDs could be stabilized either energetically, by appropriate surface treatment of confining substrates, by chirality, or by some other means. In the following we describe the general Kibble [2] and Kibble-Zurek mechanism [3], which describe the generation of TDs in a fast phase transition quench. Afterwards we describe how diverse line defect structures could be stabilized in nematic LCs confined in a plane-parallel geometry.

3.1. Kibble and Kibble-Zurekm mechanism

Generation of TDs in a sufficiently rapid continuous symmetry-breaking phase transition is described by universal mechanisms. The so-called Kibble mechanism [2], which later evolved into the Kibble-Zurek mechanism [3], was originally introduced to explain the emergence and coarsening of topological defects in the Higgs field of the early

inflationary universe. The corresponding phase transition was assumed to be of second order. It was proposed that nucleated TDs seeded the anisotropic structure of the universe, which is reflected in the anisotropic cosmic background pattern. (Later it emerged that the principal mechanism behind this were quantum fluctuations). In their modeling it was assumed that the quench rate of the phase transition mimics the inflation speed.

The key assumptions of the Kibble mechanism are that in a fast enough (i.e. quenched) phase transition the symmetry breaking choice is in general different in different parts of the system due to the finite speed of information propagation. Namely, sufficiently separated spatial regions are informationally isolated and uncorrelated. Consequently, the domain-type structure in the *phase* component of the order parameter field of the condensed phase forms, where TDs are enforced at the domain interfaces. The size of the initially formed domains (the so called *protodomains*) depends on the quench rate. Afterwards, the description of domain formation was improved by Zurek [3], who demonstrated the important role of critical slowing down. Furthermore, he proposed that due to the universality of this mechanism, condensed matter systems could be exploited as a laboratory system for understanding cosmology. The key prediction of the Kibble-Zurek mechanism refers to the linear size of protodomains $\xi_d^{(p)}$, which yields the initial concentration of TDs. Theoretical analysis reveals that it scales[3] as $\xi_d^{(p)} \propto \tau_Q^{\nu/(1+\eta)}$. Here τ_Q measures the time in which the phase transition is completed – it is inversely proportional to the quench rate – and ν and η are the critical exponents describing the amplitude order parameter correlation length and relaxation time at the phase transition. This prediction was tested and, in most cases, also confirmed in diverse condensed matter systems, such as superfluids [50,51], high-T_c superconductors [52], and liquid crystals [53–55]. For example, in nematic LCs [53,54] it roughly holds $\nu \sim 1/2$ and $\eta \sim 1$, yielding

$\xi_d^{(p)} \propto \tau_Q^{\frac{1}{4}}$ [56]. After the quench the nearby *defects* and *antidefects* annihilate, and consequently the characteristic linear size of domains monotonically increases, and the universal time scaling regime ensues. For nematic LCs (NLCs) it roughly holds that $\xi_d \propto t^{1/2}$ [57,58]. Note that the coarsening mechanism is well described by a single linear characteristic length ξ_d. Numerical simulations in NLCs reveal that coarsening dynamics in a sufficiently fast quench exhibits at least three qualitatively different stages: i) early regime, ii) domain regime, iii) defect regime [57,58]. The i) early regime is dominated by exponential growth of the order parameter amplitude. In this stage domains are not visible due to the relatively weak degree of condensed order. In ii) the domain regime, domains exhibiting different *phases* of the order parameter are visible. In the iii) defect regime, most *defects* and *antidefects* are mutually annihilated, so that instead of domain walls the structure of individual TDs dominate the structural pattern. In a purely achiral NLC a single domain is eventually established, where TDs are absent.

In the following we turn to various experimental techniques that enable stabilization of line defects in NLCs confined within plane-parallel cells.

3.2. Confinement induced stabilization

A large number of methods have been developed to effect placement of a desired topological defect or collection of defects in a liquid crystal cell. Here we review many of these, ultimately focusing on scribing a polymer alignment layer with the stylus of an atomic force microscope.

Eakin et al. [59], Crawford et al. [60], and Gorkhali [61] exploited polarized holography to pattern linear and square arrays of alternating TDs of integer ($s = \pm 1$) strength. Fleury, Pires, and Galerne adopted a more brute force approach, in which they created a TD array by rubbing the substrate with a PTFE (Teflon^{TM}) rod [62]. Despite

the ease of these methods, they tend to produce relatively widely spaced defects. On smaller scales of order a few tens of micrometers, a Colorado group led by Smalyukh adopted an optical tweezing approach: Here two scanning mirrors direct a tightly focused laser to arbitrary coordinates within the sample, thereby generating an array of torons, gratings, skyrmions, and other structures — even in three dimensions [63-66]. Yokoyama's group has adopted a maskless exposure system for photolithography in which they create 2 × 2 mm patterns with resolution approach 2 μm [67]. More recently they developed a photolithography method based on a voltage switchable liquid crystal phase mask that uses the Pancharatnam-Berry phase; they have achieved resolution of 0.5 μm [68,69]. Led by Wei QH and Lavrentovich OD, a group at Kent State developed a defect patterning technique to create three dimensional defect networks by exploiting 2D plasmon photopatterning on the two substrates of the cell [70-73]; they have used this approach for patterning both standard calamatic and lyotropic chromonic liquid crystal defects. Ware, et al, photopatterned defects in a liquid crystal elastomer with defects that can change shape under various external stimuli, giving rise to 3D liquid crystal voxels [74]. A different approach has been taken by Yoon's group, in which they judiciously applied voltages to patterned electrodes to generate patterns of desired defects [75]. Kim and Serra created regular and adjustable arrays of defects by incompletely etching electrodes, thus creating a periodic conductivity. This facilitated application of a laterally modulated electric field [76]. A similar approach was adopted by Orihara's group but using a charged dielectric layer to cover the electrodes [77]. Orihara's group also created patterns by exploiting umbilical defects at the two substrates, adding ions, and applying an ac electric field [78]. A joint Dutch/Slovenian group used chemical/optical patterning [79]: They deposited a homeotropically-orienting silane onto a substrate, then optically etched away spatially

periodic square regions to create an array of planar-aligning squares in a hometropically aligning “sea”. They subsequently used this surface to create skyrmion-like defect patterns. Mechanical approaches for defect patterning are several. A joint Chinese/Hungarian/Japanese team used a “dragging” technique to create a dynamically formed array of TDs at large scales by coupling a group of TDs to a dragging force, which sorts and orders the TDs [80]. Stannarius’ group created desired patterns of defects on free-standing films by physically poking the film with a tiny probe [81]. Serra exploited a regular array of micro-pillars, sometimes in conjunction with electric fields, to create controllable defect arrays [82,83]. Surface topographies in a photoresist also have been used by a group in Stuttgart to create defects in chromonic liquid crystals using two-photon laser writing process [84].

Each technique has its own disadvantages and advantages. On the negative side, most of the techniques, except those of Refs. 68, 69, and 79 cannot create features on the submicrometer length scale. The holography methods in Refs. 59, 60, and 61 can provide only limited types of patterns, and both the optical tweezing (Refs. 63-66) and mechanical poking (Ref. 81) approaches te Topological Point Defects of Liquid Crystals in Quasi-Two-Dimensional Geometries nd to be limited in range. Chemical patterning (Ref. 79) has limited utility in controlling the spatial variation of the director. None of these techniques, except the micro-pillar array (Refs. 82 and 83) and optical tweezing, presents a viable means of controlling both azimuthal and polar orientations of the director. But on the positive side, many of these techniques, most notably the 2D plasmon photopatterning technique (Refs. 70-72), allow for rapidly-created large area patterns. Moreover, most of the approaches that do not involve mechanical contact motion with the surface are “clean”, in that there is no residue.

In this article, however, we shall focus on mechanical nanoscribing utilizing the stylus of an atomic force microscope (AFM), the approach of which, as well as advantages and disadvantages, are described below. More than twenty-five years ago Rüetschi, et al demonstrated that scribing a polymer surface with an AFM stylus creates an easy axis for planar nematic alignment [85]. Based on this principle, Yokoyama showed that tiny regions can be scribed to exhibit tristable switching behavior [86], effectively a forerunner of defect patterning. At about the same time, Rosenblatt's group demonstrated that AFM scribing can be used to create an ultrahigh resolution display having a gray scale [87], as well as initial work on liquid crystal optical gratings [88]. The principle is straightforward: A polymer such as polyvinyl alcohol (PVA) or a commercial polyimide is deposited on a substrate, and the AFM stylus is programed to scan a predetermined pattern in in contact mode, where both the in-plane (azimuthal) direction and the scribing force can be varied point-by-point. As is the case with cloth rubbing of a polymer alignment layer, the alignment of the liquid crystal director is due to a combination of entropic considerations due to the nano-grooves that are created by the scribing process, and anisotropic dispersive interactions between the liquid crystal and the now partially aligned polymer backbone and side groups [89,90]. There are numerous advantages to such a scheme, the most important being the tiny features that can be achieved. With spacing between rub lines being as small as the tip of the stylus – this is typically of order 10 – 20 nm – one can realise features that generally are not accessible by other means. For example, one can divide "super" pixels into much smaller subpixels and control the overall properties of the super pixel (orientation, anchoring strength) by spatially averaging over the properties of the subpixels [91]. Another major advantage is the ability to control not only the azimuthal component of the director at the surface, but the polar angle as well. In principle this can be

accomplished by using appropriate alignment layer polymers that provide a wide range of continuous pretilt angles [92,93], ideally from planar through homeotropic alignment, and then varying the contact force of the stylus. Preliminary data were obtained by scribing a mixture of polyimides SE-1211 (which produces homeotropic alignment) and RN-1175 (which produces planar alignment), both from Nissan Chemical Industries. By overbaking and scribing with an AFM stylus, simultaneous azimuthal and polar (from hometropic to 70^{o}, i.e. nearly planar) alignment control was achieved [94]. Results of this sort may also be obtainable from ion beam bombardment of mixed polyimide surfaces, although with somewhat less spatial resolution [95].

Nevertheless, there also are disadvantages to AFM scribing. Perhaps the most important issue is the overall size of the pattern and the time involved in scribing. Patterns typically are limited to approximately 100 μm on a side, which requires several minutes of scribing, depending on the complexity of the pattern. Multiple patterns can be tiled together, but the serial nature of the scribing process adds to the time involved. Another issue is the creation and disposal of debris that can attach to the stylus during the procedure. Nevertheless, AFM scribing remains an efficacious tool because of the rapid turnaround times to modify a pattern and the ability to achieve high resolution and control both polar and azimuthal orientations simultaneously.

3.3. AFM Scribing Method

For a typical surface defect of strength *s*, Nehring and Saupe used the equal elastic constant approximation and assumed planar anchoring to obtain the solution to Laplace's equation, given by Eq.(13) [96]. Notice that ψ is independent of *r* in the equal elastic constant approximation. Because $\hat{\boldsymbol{n}} = -\hat{\boldsymbol{n}}$, only half-integer and integer values of *s* are permitted: $s = \pm \frac{1}{2}, \pm 1, \pm \frac{3}{2}, \pm 2, \ldots$. Moreover, topological constraints require

that half integer singularities necessitate that the director be planar [96]. The director orientations ψ_i are summed over the entire two-dimensional surface when multiple defects are present, which allows one to express the director orientation in Cartesian coordinates using Eq.(14).

In principle one can convert $\psi(x,y)$ into a series of continuous lines spaced some arbitrary distance apart when programming the instrument to scribe these lines into a polymer surface. Of course, higher pattern resolution can be achieved by reducing the spacing t between lines, at least until any debris from one line begins to be deposited into the adjacent lines. (This is more prevalent when the polymer is soft, and the scribing is forceful.) Another issue with which one must contend is the induction of an unwanted pretilt angle away from planar orientation. The latter problem can be circumvented by alternating or randomizing the directional sense of scribing from one line to the next, as was implemented by Murray et al. [97]. They also dealt with the former problem by varying t with the local curvature: In regions of high curvature, Murray et al. used tight line spacing t, whereas they increased the spacing in regions where the director is relatively uniform.

To create a quasi-2D director profile through the cell, one can scribe a mirror image on a second substrate and bring the two patterns into register using, eg. a mask aligner normally used in photolithography. The lowest practicable alignment registration is ~ 1 μm with this technique. Alternatively, and this is the approach adopted by Murray et al. [97], one can use an unpatterned planar degenerate alignment layer, such as polymethylmethacrylate (PMMA) or 3-glycidyloxypropyl) trimethoxysilane (GLYMO) [98].

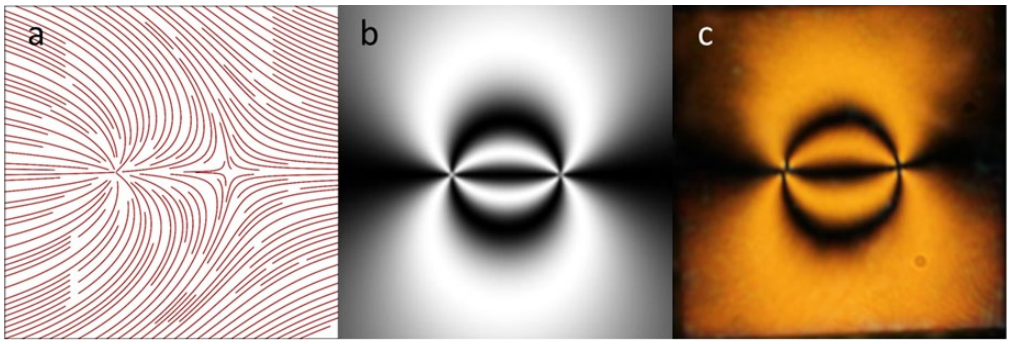

Figure 6. (a) computer-generated scribing pattern for a pair of $s = \pm 1$ defects spaced approximately 20 μm apart, where the constant c_i is set equal to zero; (b) theoretical polarized micrograph for the liquid crystal between crossed polarizers; (c) actual experimental polarized micrograph of the liquid crystal cell scribed with a high density of lines (120-300 nm line spacing). The lines were scribed at a stylus speed of 18 μm/s and with a force of 3 μN.

In this case the patterned surface serves as a master from which the orientational order is transmitted through the cell thickness, becoming locked in at the planar degenerate surface. Of course, the cell thickness d needs to be thinner than the features of the pattern to prevent the director pattern from becoming washed out through the cell. Figure 6 shows the results for a pair of $s \pm 1$ defects (with phase $\psi_0 = 0$, see Eq.(11)). In principle any defect pattern can be created, as seen, for example, in Figure 7. Kralj et al. published a polarized optical microscope image of a 3×3 array of $s = \pm 2$ defects [99], similar to the one shown in Figure 7.

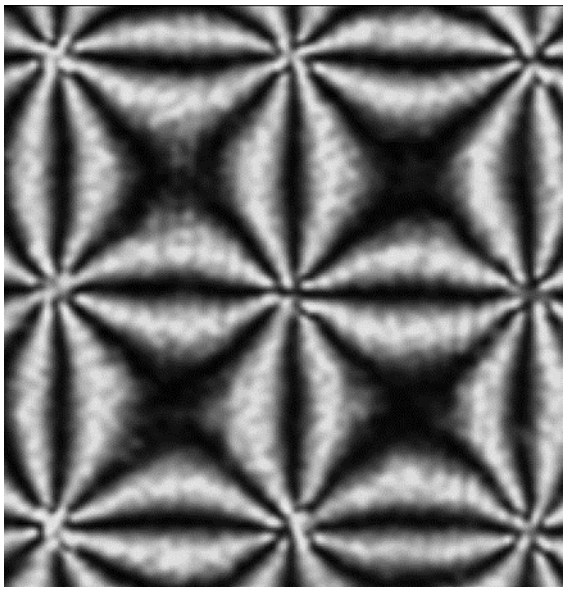

Figure 7. Polarizing Optical Microscope (POM) image of an array of s = ±2 defects. Defects are spaced approximately 30 μm apart.

4. Stabilization and Manipulation of Topological Defects

The patterning of defects facilitates a variety of studies. For example, one can examine more easily the structure of the defects, and the ability to alter the structure with applied fields without concern of defect mobility or pairs of oppositely charged defects undergoing mutual annihilation [100]. One also can create quasi-in-plane line disclinations terminating at the fixed surface defects and manipulating them with an electric field to create an "alphabet" of observable patterns [101]. One can examine dimensional crossover behavior [102], and even observe unexpected results such as the co-revolution of half-integer defects about a central point [103,104]. Here we discuss some of these phenomena.

4.1. Structure of Defects

There are several mechanisms that can relieve the strain energy associated with an integer topological defect. The defect can decompose into a pair of half-integer defects [97] or escape of the director into the third dimension (Figure 8) [105,106].

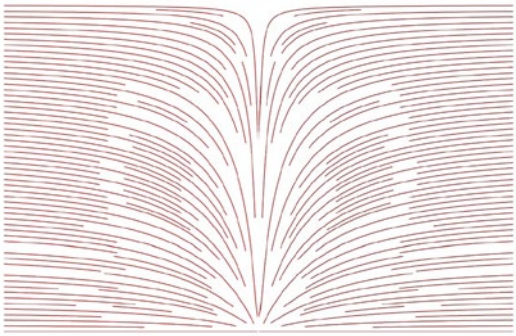

Figure 8. Schematic of director field for a fully escaped s = +1 defect. Notice boojums at the top and bottom substrates.

In a theoretical study, Chiccoli et al. [107] estimated the free energy of a pair of strongly anchored (split) half-integer defects to be $F_{pair} = \pi K d\left[\frac{1}{2} ln(2R^2/rL) + 2u\right]$, where K is an elastic constant; d is the cell thickness; R is a characteristic domain size; L is the gap between the split defects; r is a molecular size; and u is the normalized defect core energy. They calculated the energy to be $F_{esc} = \pi K d[ln(R/d) + g]$ for a fully escaped integer defect, where g is a constant ~ 4.1. Thus, the two mechanisms are both weakly sensitive to d. Moreover, they found that s = ±1 defects in uniaxial nematic cells always escape when d > 200 to 500 nm, and that defect splitting into pairs of half-integer defects does not occur. Regarding biaxiality, they found that escape is common for weakly biaxial nematics but splitting tends to occur when biaxiality is strong.

To examine some of these issues, Murray et al. used AFM scribing to create regular arrays of surface defects in thin cells containing the positive dielectric aniostropy liquid crystal pentylcyanobiphenyl (5CB), which they examined using polarized microscopy as functions of d and applied voltage [100]. As predicted by Chiccoli, et al, they found that thinner cells (d ~ 3 μm) tend to favor decomposition of integer defects into pairs of half integer defects, i.e. of strength s = ±½. They found that on heating/cooling cycles between nematic and isotropic phases, some apparently split

defects can morph into unsplit integer defects, or vice versa. This observation is consistent with the similar logarithmic energy forms in Ref. 107, and also hints that the structural transition is first order; this is behavior that will be discussed later. Because they used a positive dielectric anisotropy liquid crystal, an electric field applied normal to the substrate (utilizing indium-tin-oxide (ITO) electrodes) would tend to drive the director out of the cell's plane and along the z-axis. In fact, in the thinner cells Murray, et al generally observed a sharp Freedericksz transition on applying this voltage, whereby *dI/dV* – here *I* is the intensity of the transmitted polarized light – changes abruptly with increasing voltage just beyond the defect cores. This behavior is indicative that pairs of half-integer defects are present, where topological constraints force the director to lie in the xy-plane in the absence of a field. As noted above, outside the defect core, thicker cells ($d > 6\ \mu$m) tend to favor escape of the nematic director. Murray et al. gleaned this behavior from the absence of a well-defined Freedericksz transition threshold in these regions: Rather, *dI/dV vs. V* displayed a strongly rounded profile [100].

Murray et al. obtained additional information utilizing an electric field. For the escaped radial (ER) defects, dark rings were observed to surround the defect core wherever the optical retardation α [$\equiv \int_0^d 2\pi\Delta n(z)/\lambda dz$] equals an integer multiple of 2π. Here $\Delta n(z)$ is the local birefringence and λ is the wavelength of light. By examining the progression of the dark rings, which moved inward as the electric field was increased (and the *z*-component of the director orientation everywhere increased), they were able to deduce the director orientation at the core of the escaped radial defect. They found that the escape was not complete, i.e. the director $\hat{\boldsymbol{n}}$ possessed a radial component even at $r = 0$ [100].

Topological constraints require that the director must lie in the cell's plane in the regions in and around pairs of $s = \pm 1/2$ defects. Murray et al. were able to heat the sample to a temperature at which the retardation α vanished nearly everywhere, and the cell was dark under crossed polarizers - except near the cores of the defects [100]. The reason for the brighter appearance near the defect cores is because the disclination lines are not aligned completely along the *z*-axis, but instead possess an in-plane component. This is because the half-integer defects are more strongly pinned at the pattern substrate but remain somewhat mobile at the opposing planar degenerate substrate. Owing to the mutual repulsion of the half-integer defects, there is an in-plane component of the disclination line, resulting in an effective retardation $\alpha \neq 2\pi$. By examining the intensity of these spots Murray et al. were able to deduce the angle made by the disclination line with respect to the z-axis [100].

4.2. Defect switching

As discussed above, there are a variety of ways that an $s = +1$ surface defect on opposing substrates, and the intermediate disclination line, may relax the total energy: biaxial order reconstruction [108,109], core melting, director escape [105,106,110], and decomposition into a pair of $s = +1/2$ defects [100]. The latter two are the most commonly observed and have been the subject of the most active investigations. As described above, sample thickness has been a major focus in these studies, and defects can interconvert between escaped and split on heating into the isotropic and recooling into the nematic phase [100]. An important issue is whether these interconversions can occur *via* a continuous process, or whether an intermediate melting of the defect core occurs, indicative of a discontinuous pathway in which the two end states are topologically distinct. To examine this question, Susser et al. patterned an $s = +1$ defect that gave rise to an escaped radial director profile for a negative dielectric anisotropy

liquid crystal [103], i.e. $\Delta\varepsilon < 0$. They applied an ac electric field, which has the effect of driving the director into the *xy*-plane. Importantly, once the director field lies nearly in the *xy*-plane, it becomes possible for the defect to decompose into a pair of +1/2 defects. For the discontinuous pathway, the symmetry in the escaped radial core must change from positive to negative uniaxial via melting at some specific threshold field. This permits the appearance of an $s = +1$ defect, which subsequently splits into a pair of +1/2 defects, the core of which relieves the imposed frustrations via order reconstruction [43] as an intermediate step. For a continuous pathway, strong planar anchoring at the patterned surface would permit splitting of the ER defect to occur at that surface – this is because the director already lies in the *xy*-plane at the surface due to the strong anchoring – resulting in an elongated disclination arch between the two surface defects. This arch would rise to the opposing surface with increasing electric field until it makes contact with the that surface, resulting in a pair of independent half-integer defects. They also studied the reverse process (split pair to a single escaped defect), in which a positive dielectric anisotropy liquid crystal is used.

Using the Merck liquid crystal materials ZLI-4330 ($\Delta\varepsilon < 0$) and 5CB ($\Delta\varepsilon > 0$), Susser et al. performed optical measurements and found that there is well-defined threshold field at which the transitions occur [103]. Moreover, there was no indication of the arched disclination that would be required for the continuous pathway. They also carried out numerical simulations, which were in good quantitative agreement with the experimental results. From their observations, they concluded that the interconversion between escaped radial and a pair of split half-integer defects is discontinuous, with core melting as an intermediate step and with the two end states being topologically distinct.

4.3. Co-Revolving defects

In their work to elucidate the interconversion from an $s = +1$ escaped radial defect to $s = +1/2$ defect pairs, and vice versa, Susser et al. observed that the half integer defects co-revolve a common central point when the electric field is above some critical value [103]. More recently they examined the origin of this phenomenon in more detail [104]. Figure 9 shows a pair of these counterclockwise co-revolving half-integer defects in an applied electric field $E = 6.5$ V m^{-1} at frequency $\nu = 250$ Hz. The images are temporally spaced 1/15 s apart and the bar corresponds to 10 μm.

Perhaps their most important observation is that the phenomenon occurs only for negative dielectric anisotropy liquid crystals. This immediately suggests that the co-revolution is related to the ubiquitous electrohydrodynamic (EHD) instability often known as the Carr-Helfrich (C-H) instability [111-113]. Based upon this observation, Susser et al. investigated the co-revolution as functions of both applied electric field and frequency of the applied field [104]. Moreover, they studied the behaviour of the EHD instability, which also can be seen as "ripples" in Figure 9. Some of their salient observations are:

i. At low fields neither the EHD instability nor the co-revolutions are present.

ii. Above some frequency-dependent threshold field they observed stationary C-H domains. At approximately the same field they began to observe "wobble" of the defect pair, as the azimuthal coordinates of the defects would fluctuate antipodally about some central point. They measured the rms amplitude $\left\langle \Delta\varphi^2 \right\rangle^{1/2}$ and period of this wobble vs. applied frequency ν.

iii. At still higher fields they found that the wobble was interspersed with half and full revolutions of the defect, which set in at approximately the same field as the movement of the C-H domains.

iv. At a still higher field E_{rev3} they found that the defects co-revolve at an angular frequency ω that is related to both the field and applied frequency ν. E_{rev3} was found to be proportional to $\nu^{1/2}$.

v. At a fixed field above E_{rev3} the angular frequency ω was not always stable. Instead, it could hold some value for a few seconds, then jump to a different value, and then jump again. This was not explained in their work, but we believe that it may be due to the phenomenon of intermittency that may occur in dynamic systems [114].

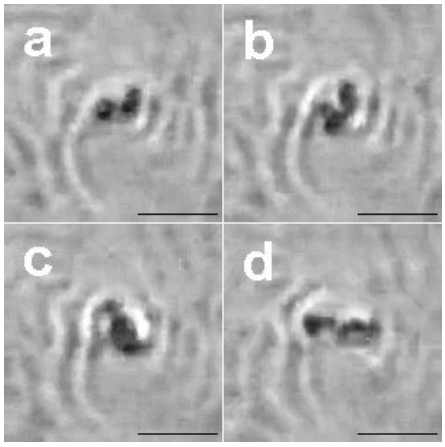

Figure 9. Co-revolving defects. See text for details. Here the liquid crystal is Merck ZLI-4330.

Susser et al. developed an E-ν phase diagram in which they superimposed the co-revolution and the EHD behaviours, finding strong overlaps. From these results they speculated that the phenomenon is analogous to the Lehmann effect, in which cholesteric liquid crystal droplets rotate when there is a temperature gradient along the cell normal [115]. For the co-revolving defects, they suggested that the EHD instability induces chirality in the system and that it is instrumental in creating charge flow. The latter effect, in addition to the mechanical field stress from the EHD instability, serves an analogue for thermal flow in the classical Lehmann effect. Nevertheless, at this time there is no detailed theory for the co-revolution.

4.4. "Wiring" of Defects: Reconfigurable Multistable Defect Patterns

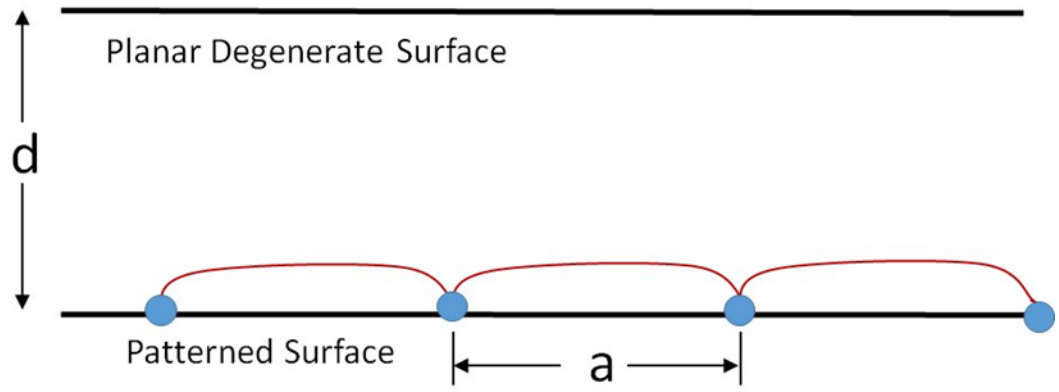

Figure 10. Schematic diagram showing the end-on view of defects. For $d > \sim 0.5a$, the defects run along the patterned and terminate on the nearest neighbour defect of opposite sign. The $s = \pm 1$ patterned defects, which have decomposed into pairs of +1/2 or -1/2 surface defects, are shown in blue. The disclination lines (in red) run between an $s = +1/2$ defect at one site and an $s = -1/2$ defect at the adjacent site.

To this point the discussion has centred on disclination lines that emanate from a defect at one surface and traverse the cell thickness to terminate at the opposing substrate. This occurs when the cell is sufficiently thin, typically $d <$ the in-plane spacing a between defects. For thicker cells, the energy cost of the disclinations starting and terminating on the same substrate is smaller, and the defects can follow approximately the trajectory shown in Figure 10. Calculations [116] predict that the crossover from in-plane to defects normal to the surface occurs when $a/d \sim 1.1$, although this will depend on the nature of the surface anchoring and the relative elastic constants. Based on this idea, Harkai et al. examined a square 4 × 4 lattice of alternating $s = +1$ and -1 patterned defects that decompose into half integer defects [101]. The in-plane spacing was approximately 20 μm, and when forming a cell with the opposing substrate being treated for planar degenerate alignment, the cell gap d was 16 μm. On filling the cell

with 5CB, disclination lines were observed to run between adjacent defects, despite *a/d* being of ~ 0.8.

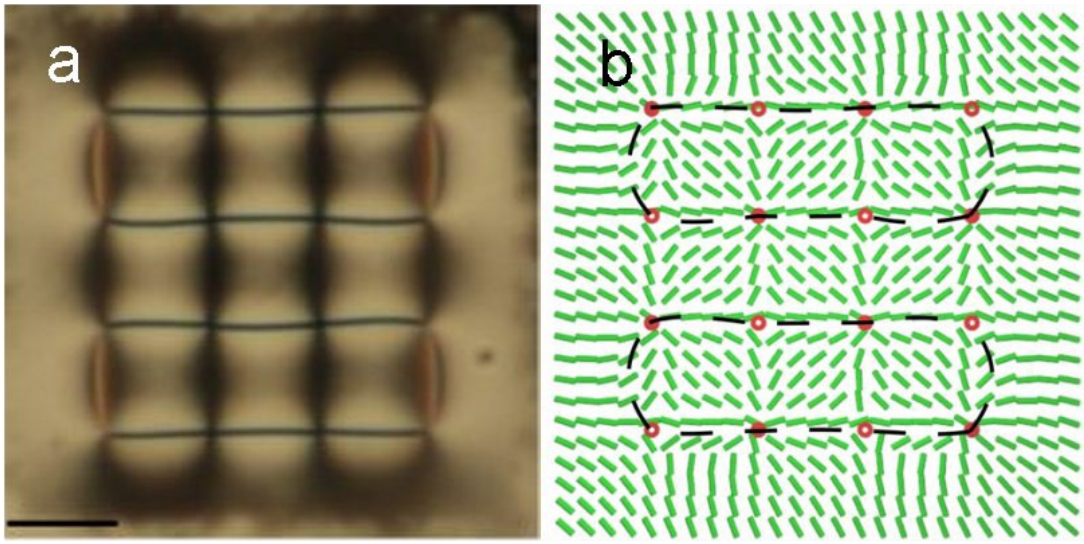

Figure 11. a) Polarizing microscope image of typical disclination viewed between polarizers. Black bar is 20 μm. [After Ref. 101], b) Schematic representation of the disclination pattern in which chargeless defects connect nearby split s=1 (full red circles) and s=-1 surface defects (open red circles).

Numerically calculated nematic textures exhibiting seven different symmetries emerging from the enforced 4 x 4 array of alternating $s = \pm 1$ surface imposed defects. Left: The top cell view of the line defect patterns where regions with strongly suppressed order parameter values are shown. The solid and open circles indicate origins of nucleating *s*=+1 and *s*=-1 defect sites. Right: The corresponding typical optical microscopy textures obtained under crossed polarizers [After Ref. 101].

In order to manipulate the disclination lines, Harkai et al. arranged two pairs of in-plane electrodes so that a field could be applied along the *x*-axis or the *y*-axis. Figure 11 shows the pattern at zero applied field after an ac electric field had been applied for some time along the *y*-axis, i.e. vertically in the figure, and subsequently

brought back to zero. A field was then applied along the *x*-axis, and Figure 12 shows a series of images of disclination line with successively increasing fields. Figure 12c shows the penultimate configuration: For larger fields no further change is observed.

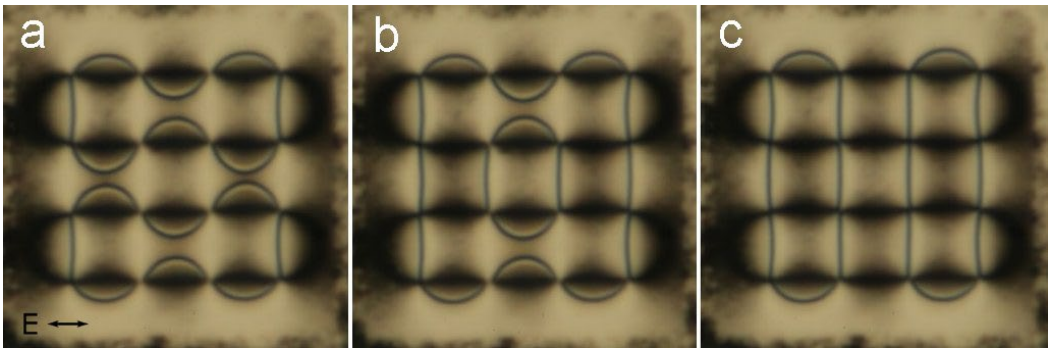

Figure 12. Disclination patterns on increasing the electric field applied along the x-axis. The configuration in *c* is achieved at the highest applied field. [After Ref. 101]

Importantly, each configuration is stable, that is, on reaching a configuration such as in Figure 12(a) or Figure 12 (b) and reducing the field to zero, that configuration remains stable. One would need to increase the field further to achieve a different arrangement (culminating in Figure 12c) or apply an electric field along the orthogonal (*y*) axis.

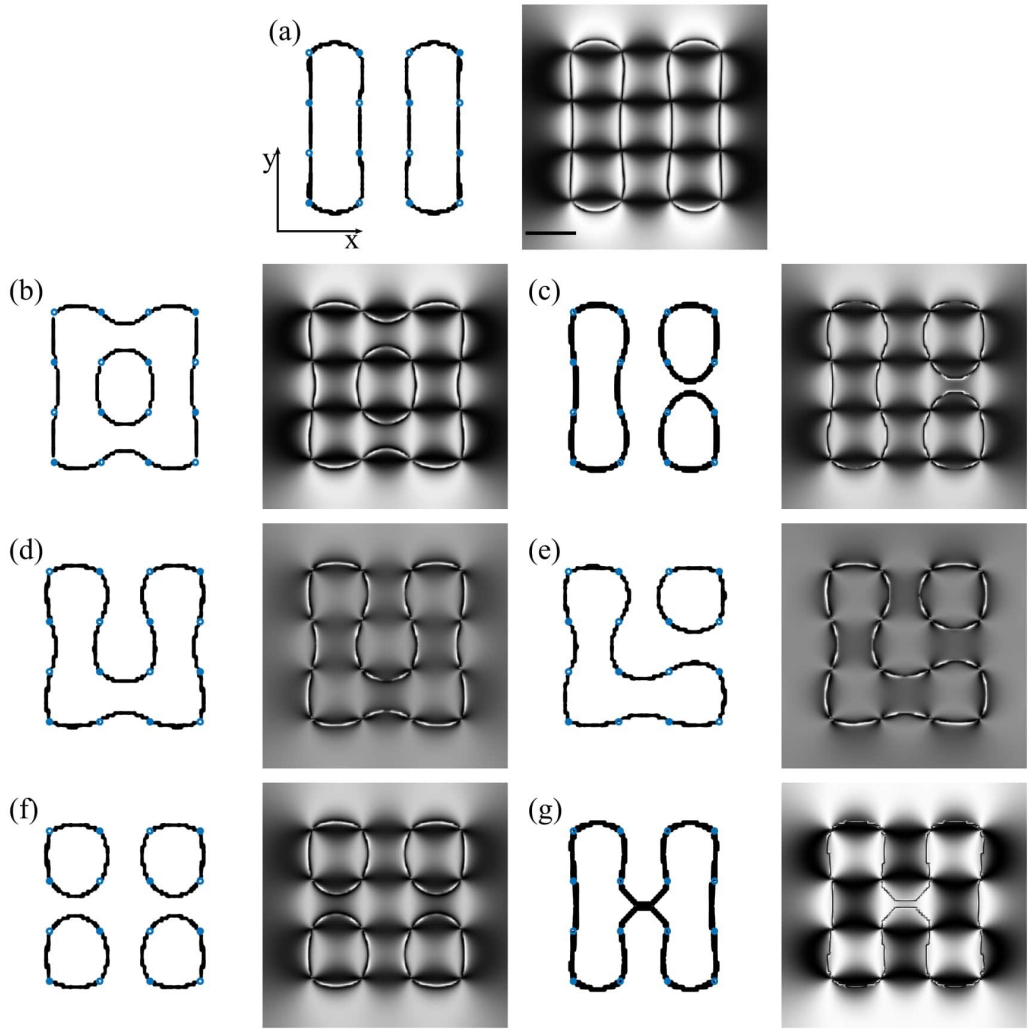

Figure 13. Numerically calculated nematic textures exhibiting seven different symmetries emerging from the enforced 4 x 4 array of alternating $s = \pm 1$ surface imposed defects. Left: The top cell view of the line defect patterns where regions with strongly suppressed order parameter values are shown. The solid and open circles indicate origins of nucleating *s*=+1 and *s*=-1 defect sites. Right: The corresponding typical optical microscopy textures obtained under crossed polarizers. [After Ref. 101]

In Figure 13 we plot all possible (meta) stable configurations of chargeless disclinations enabled by an imposed 4×4 array pattern of alternating $s = \pm 1$ surface defects in relatively thick cells, so that the dislocation lines are confined within the master substrate. The structures were obtained numerically by minimizing the free energy of the system

[101]. We plot only the disclination lines (i.e. cores of defects, where the nematic order is strongly suppressed) in the *xy*-plane perspective and the corresponding interference patterns, simulating the optical polarized microscopy experiment under crossed polarizers. Each line defect in the figure connects a pair of nearest-neighbor daughter defects of opposite sign. This setting enables an "alphabet" of 18 different disclination configurations and in Figure 13 we show only seven *irreducible* configurations, exhibiting different symmetries. All other patterns can be obtained from this set via rotations. Note that one can transform between different disclination configurations by rewiring just few pairs of facing disclinations.

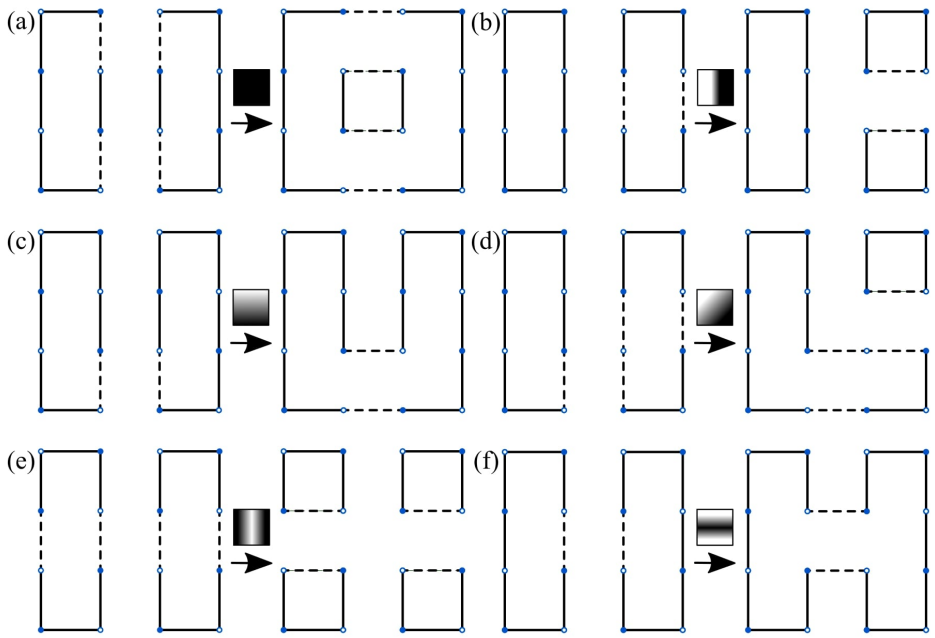

Figure 14. Schematic representation of rewiring between different irreducible patterns. Disclinations marked by dashed lines are rewired during the transformation. This may be accomplished by using a spatially-dependent electric field. The coloured squares above the arrows schematically indicate the spatial profile of the external electric field ***E***. Black and white colours mark a relatively large and zero value of *E*, respectively. The diffuse regions correspond to spatially slow variation of field ***E***.

In Figure 14 we schematically sketch how all members of the irreducible set could be reached starting from the configuration shown in Figure 13(a). In the figures we indicate rewiring lines by dashed lines. For each transformation we sketch the spatial profile of the in-plane electric field, which enables this transformation, where the magnitude of the field is related to darkness of the colour. Note that all patterns are found to remain stable after the transformation-enabling electric field is switched off.

There are numerous applications for these electrically re-wireable line defects. For example, they could be used to trap nanoparticles or nonlinearly control electrical conductivity. They could be used as controlled nano or microwires, or even for applications as prosaic as multi-stable signage (Ref. [101]).

4.5 Electric field-induced 3D to 2D crossover of disclination lines

As we have seen above, disclination lines may terminate at defects on the same substrate or on opposing substrates. The work of Harkai et al. demonstrated how quasi-in-plane disclination lines may be "rewired" with an in-plane electric field [101], where the director field that surrounds the disclination is key to manipulating the disclinations. But importantly, disclination lines that connect an $s = +1/2$ and $s = -1/2$ ("opposite sign") surface defect are qualitatively different from a disclination that connects a pair of $s = +1/2$ ("same sign") surface defects, as can be seen in Figure 15. Figure 15a shows a schematic representation of a disclination line that connects a pair of opposite sign defects, which corresponds to the approximate lowest energy state as calculated by Afghah et al. [117]. Notice that the director field surrounding the disclination line remains in the *xy*-plane, i.e. the director field is two-dimensional. On the other hand, the director field surrounding the disclination that connects a pair of same sign defects in Figure 15b is fully three-dimensional, with an $s = -1/2$ defect at the apex of the disclination being the lowest energy configuration. These sorts of differences were

discussed previously by Kleman and Lavrentovich [4] and by Mermin [1], although the theoretical work of Afghah et al. [117] and experimental work of Ferris et al. [102] focus on the actual crossover of the director field from three to two dimensions in the presence of an electric field.

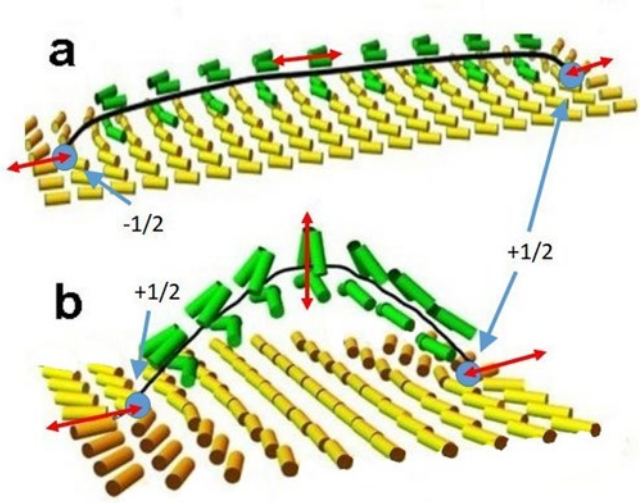

Figure 15. Schematic representation of the disclination lines and associated director fields in the presence of: a) a pair of opposite defects of strength ±1/2 and b) same sign defects of strength +1/2, as shown by the blue dots. The red double-headed arrows represent the director symmetry axes at different points. Notice along the disclination line in (a) that the director at the apex lies in the xy-plane, but in (b) the director lies along the z-axis (Courtesy of A.J. Ferris).

Consider a negative dielectric anisotropy liquid crystal, whose director's lowest energy state is perpendicular to an electric field. If the field is applied along the *z*-axis, the director field along the disclination in Figure 15a. remains largely unperturbed, as it already lies mostly in the *xy*-plane everywhere in the cell. On the other hand, the director field in Figure 15b will be pushed into the *xy*-plane, which requires an increasing z-component of the disclination trajectory. The only way to accomplish this

is for the disclination arch to extend upward toward the opposing substrate. Afghah et al. [117] predicted and Ferris et al. demonstrated experimentally [102] that this indeed occurs, where for sufficiently large field the disclination makes contact with the opposing substrate and splits. This would leave a pair of unconnected disclination lines extending from each of the two same sign defects on the patterned substrate to the other substrate. For each of these disclination lines, the now 2D director field is perpendicular to the line and therefore lies in the *xy*-plane. The results show that disclination lines surrounded by a 3D director field can connect any pair of half-integer surface defects, as these disclinations can be topologically transformed. The 2D director field, however, cannot transform continuously because the related disclination lines are topologically inequivalent. Thus, only certain defect pairs can be connected *via* a disclination line surrounded by a director field that lies in the *xy*-plane. Because a pair of $s = +1/2$ defects cannot be connected by the 2D director field, the 3D disclination arch is ejected on application of a strong electric field, which forces the director to adopt a 2D configuration.

5. Chirality and nanoparticle-driven stabilization

Next, we consider chiral LCs. Strong enough chirality could stabilize blue phases (BPs), which exhibit lattices of disclinations. These structures could be nucleated by double-twist excitations, which tend to establish locally double-twist cylinders (DTC). We first analyse suitable LC elastic conditions for such configurations. Afterward, we report how the stability of such structures could be manipulated by using appropriate nanoparticles.

5.1 Stabilization of double-twist cylinder units

The representative double-twist - type mode is parametrized in cylindrical coordinates $\{\varrho, \varphi, z\}$ by [38,118,119]

$$\hat{\boldsymbol{n}} = -\hat{\boldsymbol{e}}_{\varphi} \sin(Q\rho) + \hat{\boldsymbol{e}}_{z} \cos(Q\rho). \quad (13)$$

It is characterized by the periodicity Q [118], which is in BPs comparable to the value of inherent LC chirality parameter q_{ch}, which corresponds to 2π/pitch of the helix. Note that DTC structures are in addition to chirality favored also by the saddle-splay elasticity. Namely, the corresponding elastic free energy term in a cell of thickness *d* yields [118]

$$F_{24} = -2\pi K_{24} d \sin^2(QR), \quad (14)$$

where Eq.(13) is used and *R* stands for the radius of the cylindrical LC body. In the case of the so-called meron structures, which make the basic unit element of a BP structure confined to a sufficiently thin cell [118-121], it holds that $QR = \pi/2$ and $F_{24} = -2\pi K_{24} d$. For example, in samples characterized by $K_{24} \sim 10^{-12}$ J/m and $d \sim 100$ nm, we find that $\frac{F_{24}}{k_B T} \sim 10^5$ at a room temperature *T*. Therefore, the free energy gain of this excitation is large with respect to thermal fluctuations.

For the case of meron DTC structure, it can be visualized why disclinations need to be introduced to satisfy the imposed orientational frustrations. The schematic illustration in Figure 16. shows a lattice of merons within the *xy*-plane, where the local meron structures are described by Eq. (13). Note that the total winding number within the whole *xy*-plane should equal zero. This is apparent by focusing on a representative "topologically neutral" region within the dashed rectangle. One finds two singular *s*=-1/2 disclinations and one non-singular escaped *s*=1 structure, which are locally

described by Eq.(13). One sees that meron-packing leads to singular disclinations at boundaries separation DTCs.

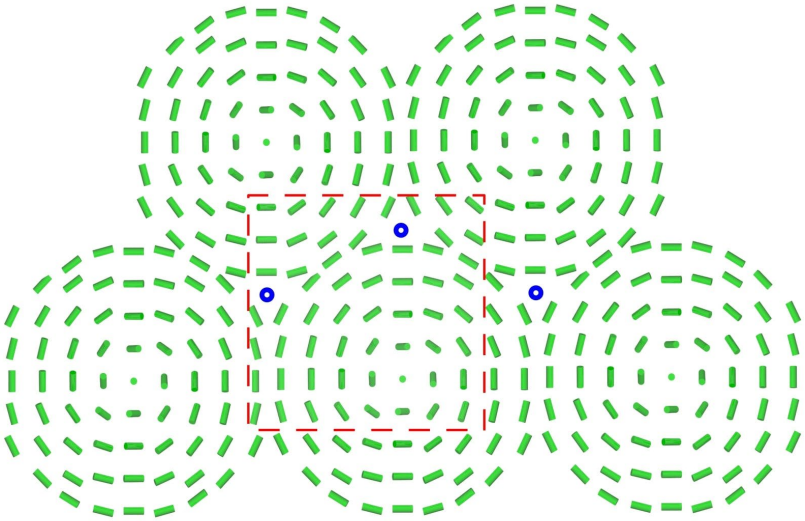

Figure16. Schematic structure of a lattice of merons shown in the *xy*-plane. The dashed rectangle represents a chargeless "lattice unit", consisting of an escaped *s*=1 nonsingular defect and two *s*=-1/2 singular defects.

Note further, that the saddle-splay elasticity promotes non-splitting of the escaped *s*=1 structure. For this purpose, we express the saddle splay free energy elastic contribution as [4]

$$f_{24} = -K_{24}\nabla.(\hat{\boldsymbol{n}}\nabla.\hat{\boldsymbol{n}} - (\nabla\hat{\boldsymbol{n}})\hat{\boldsymbol{n}}) = -2K_{24}K_G. \quad (15)$$

Here K_G stands for the Gaussian curvature of a hypothetical surface characterized by its surface normal pointing along $\hat{\boldsymbol{n}}$. Several 2D studies demonstrate [122-126] that surface patches exhibiting $K_G > 0$ ($K_G < 0$) attract defects bearing *s*>0 (*s*<0). Note further that the K_{24} contribution renormalizes the local temperature. Namely, it roughly holds [4,33] $K_{24}{\sim}LS^2$. Focusing on the quadratic condensation term and the saddle-splay elastic

term Δf close to the isotropic to nematic phase transition, where quadratic terms in S dominate, it follows that

$$\Delta f = a_0(T - T^*)S^2 - 2K_{24}K_G = a_0\left(T - T^*_{eff}\right)S^2, \quad (16)$$

where $T^*_{eff} = T^* + \frac{2L}{a_0}K_G$. Therefore, the effective local transition temperature is due to the saddle-splay term shifted by $\Delta T \sim \frac{2L}{a_0}K_G$. Consequently, within the central DTC regions (which host s=1 nonsingular structures) the transition temperature is locally increased, which favors condensation of nematic order, and disfavors splitting into pairs of two singular s=1/2 disclinations.

5.2 Nanoparticle-driven stabilization and manipulation of disclination lattices

We next focus on the stability of liquid-crystalline blue phase (BP) configurations. BPs host qualitatively different disclination lattices, exhibiting periodicities in the visible wavelength regime. Consequently, they could be exploited in various applications, particularly in photonics and tunable soft lasers [127,128]. However, BPs are stable only in a narrow temperature interval, which limits severely their applicability. For this purpose, it is of interest to identify mechanisms that efficiently widen the BP temperature stability range [17,18]. In this review, we consider nanoparticle-driven stabilization mechanisms.

The pioneering research in this direction was performed by Kikuchi et al. [17]. In their work, they stabilized BPI over a wide temperature range by assembling polymer chains within the disclination lines. NP-driven stabilization was first demonstrated by Yoshida et al. for a mixture of liquid crystals [129] by means of Au NPs with a diameter of 3.7 nm. NP-driven stabilization in single liquid crystal compounds was reported by Karatairi et al. [18] and Cordoyiannis et al. [130]. The majority of studies suggest that that optimal results are achieved by using sufficiently small [131] (less than 100 nm) and

appropriately surface-treated [132-134] NPs. These studies indicate that spherical NPs are efficient mostly in widening the stability regime of BPIII structure for liquid crystal compounds exhibiting all three BPs. Several investigations focused on the impact of NPs geometry on stabilization, where researchers used reduced-graphene oxide [135] (r-GO), MoS2 [136], laponite nanoplatelets [137], and reduced-graphene oxide additionally coated with CoPt NPs [138] (CoPt-coated r-GO). The anisotropic NPs prove to be more efficient in increasing the stability range of BPI. In Table 1 we summarize the impacts of different (spherical and anisotropic) NPs on the stability of BP phases. In Figure 17 the maximum achieved range of BPs for various NPs dispersed in liquid crystal CE8 are schematically depicted. In all these studies, high-resolution ac calorimetry and polarizing optical microscopy have been combined to determine stability range of BPs [139]. Some representative heat capacity profiles and typical BP textures visualized in these studies are presented [133,138,139] in Figure 18**.**

Table 1. The blue phase range obtained for various types of spherical and anisotropic nanoparticles dispersed in chiral liquid crystal CE8 is presented: CdSSe quantum dots[133], spherical Au nanoparticles [139], MoS_2 nanoplatelets [136], laponite clay nanoplatelets [137], r-GO nanosheets [135], CoPt-coated r-GO nanosheets [138].

Nanoparticle			**Blue phase**	
core	**Shape**	**average size (nm)**	**total range (K)**	**most stabilized phase**
CdSSe	spherical	3.4	7.2	BPIII
Au	spherical	10	7.3	BPIII
MoS_2	nano-platelet	10	9.0	BPI
laponite clay	nano-platelet	25	6.0	BPI
r-GO	nano-sheet	50	7.5	BPI
CoPt-coated r-GO	nano-sheet	50	7.8	BPI

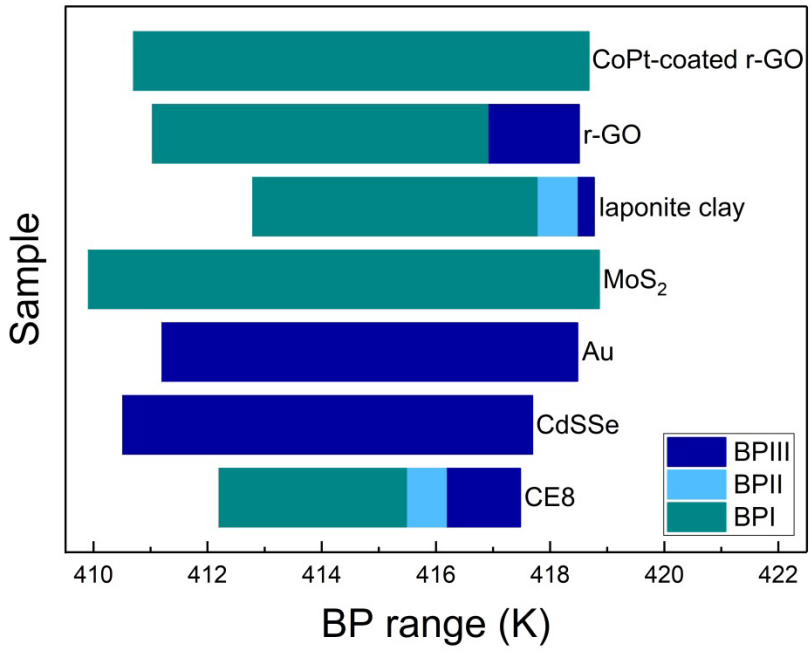

Figure 17. The range of BPs for the maximum NP concentration dispersed in CE8 is presented here; the temperature regime occupied by each of the BPIII, BPII and BPI phases is represented by different color. From the top to bottom: CE8 + CoPt-coated r-GO (χ = 0.001); CE8 + r-GO (χ = 0.001); CE8 + laponite clay (χ = 0.02); CE8 + MoS_2 (χ = 0.02); CE8 + Au (χ = 0.02); CE8 + CdSSe (χ = 0.05); pure CE8.

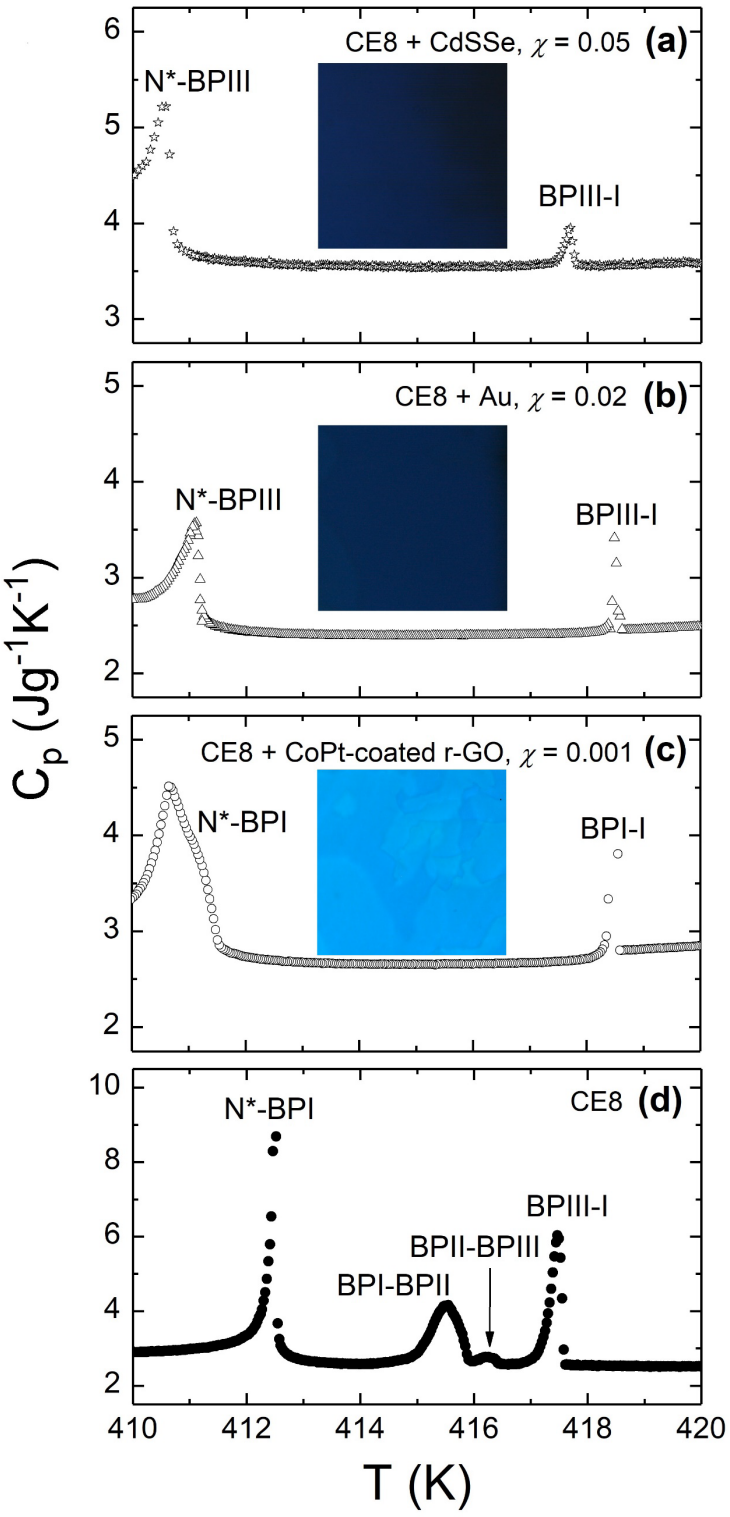

Figure 18. Representative heat capacity temperature profiles are shown for several mixtures of CE8 with NPs: CE8 + CdSSe, χ = 0.05 (a); CE8 + Au, χ = 0.02 (b); CE8 + CoPt-coated r-GO, χ = 0.001 (c); pure CE8 (d). The insets show the BP that is mostly stabilized, being BPIII for CdSSe and Au, and BPI for CoPt-coated r-GO.

The key mechanisms behind NP-driven stabilization were introduced in Refs.[17,18,134]. They are referred to as the Defect Core Replacement [17,18] (DCR) and Adaptive Defect Core Targeting [134] (ADCT) mechanism. The DCR mechanism describes the reduction of condensation free energy penalty of cores of defects by trapping appropriate NPs within them. In this way, the relatively high energy penalty of defect cores (where a structure is in general strongly biaxial) at temperatures well below the isotropic phase is (at least partially) replaced by the non-singular NP's volume. However, to achieve the stabilization [134] i) NPs should be efficiently directed towards cores of disclinations, and ii) they should not too strongly disorder the LC order parameter *phase* structure surrounding trapped NPs. First, NPs should slightly distort the LC order parameter *phase,* which enables NP to probe nearby surroundings in order to find TDs. Namely, the locally perturbed phase component typically responds on a geometrically frustration-imposed length scale. This is in general larger than the amplitude order parameter correlation length, which is typically in the nanometer scale well below the isotropic phase transition [6]. Furthermore, NPs trapped within cores of TDs should not too strongly disturb the surrounding LC structure because this introduces additional elastic free energy penalties. These penalties should not overshadow the condensation benefits owing to the DCR mechanism. The latter two conditions are the key features of the ADCT mechanism. Cordoyiannis et al. [134] demonstrated that the two mechanisms are apparently universal, since the same NPs have proven efficient in stabilizing line defects in both orientational order (disclinations in BPs) and translational order (screw dislocations in Twist Grain Boundary A phase). Note that the cores of these defects are completely different. The core of disclinations is strongly biaxial and the orientational order is relatively strongly distorted [43,44,49]. On the other hand, within the screw dislocation, the orientational order is relatively weakly distorted [4]. However, a stair-

case-like translational configuration within the defect core requires local melting of smectic A translational order.

6. Conclusions

In this review we considered diverse nematic structures enabled by the stabilization of orientational order line defects in plane-parallel confinements. One may consider bulk nematic equilibrium in achiral or weakly chiral LCs as prosaic – even uninteresting. In the achiral case one finds spatially homogeneous orientational order along a single symmetry breaking direction, and in the latter case there is a relatively simple helicoidal twisting of planar nematic planes. However, imposed geometric frustrations could energize and stabilize a rich pallete of structures. Our attention has been devoted to structures dominated by disclinations, where frustration is imposed by topological treatment of confining substrates or by chirality. We have examined the theoretical consequences of defect stabilisation; explored experimental methods to induce the desired formation of defects; focused on a number of experimental studies that involve AFM patterning of defects; and examined the effects of chirality, the blue phases, and nanoparticle capture.

Note that different numerical approaches have been used to study the core structures of individual defects and their assemblies. These involve primarily static or dynamic continuum approaches [117,140] in terms of nematic tensor order parameter as well as different lattice simulations [141,142,143]. In the latter case Brownian molecular dynamics [143] and Monte Carlo simulations [142] have been commonly employed, where both single elastic constant and anisotropic [142,143] (Frank) elastic constant cases have been simulated. These different approaches reveal robust results according to the core structure of defects: s=1/2 line defects have biaxial structure [43,44,48], and cores of point defects in general appear as a ring-like [44,46,48] nematic pattern. These

numerical results are also consistent with experimental observations, although some discrepancies [49] are reported for $|s|$=1/2 defects. These are attributed to relatively strong coupling between the amplitude and phase component of the order parameter field. Furthermore, numerical studies reveal that anisotropy of nematic elastic constants in have in most cases only qualitative effects (e.g. different core sizes and velocities of defects and antidefects [19,143] and quantitative geometric features of defect assemblies [142]) while qualitative phenomena remain robust.

The collection of diverse families of configurations "explodes" if different geometries and/or LC phases are used. For example, in chiral smectic LCs, Twist Grain Boundary (TGB) phases could be stabilized, which consist of bulk-like smectic blocks [144,145,146] separated by boundaries that host lattices of screw disclinations. Note that the TGBA phase represents a LC analog of the Abrikosov phase superconductors. In this analogy smectic screw disclinations play the role of vortices in superconductors [144]. Recent studies [138] show that the stability and structure of these defect lattices in chiral thermotropic LCs could be efficiently manipulated by doping the LC with appropriate NPs, where the same universal mechanism are exploited as in stabilization of BP phases.

Assemblies of defects, exhibiting singularities in both orientational and translational order, could be formed in Smectic-A (SmA) films covering a flat substrate enforcing tangential order, while the SmA-air interface imposes homeotropic anchoring [147]. The resulting antagonistic anchoring stabilizes the formation of periodic smectic hemicylinders, separated by grain boundaries, and hosting smectic edge disclinations. In addition, smectic hemicylinders host planar wall defects, at which smectic layer stacking suffers discontinuous reorientation. Such structures could be used to assemble appropriate NPs, the role of which is to introduce additional functionality into the system (e.g.

conducting wires [14] formed by assembled NPs). Various patterns of NPs could be formed by exploiting the trapping competition of the existing qualitatively different defect structures, i.e. crew line defects and wall defects.

Additional qualitatively new features could emerge by exploiting LC elastomers [74]. Such configurations can exhibit configurational changes through external stimuli such as bending and stretching. The resulting dynamic control of shapes may enable multifunctionality of devices. In particular, programmable shape change could be realized by controlled localized nematic order within local volume elements, which controls the inherent mechanical response. For example, one could nucleate complex 3D LC structures through programmable shape transformation of a bounding soft responsive 2D sheet [148].

Finally, colloidal particles could introduce qualitatively new LC structures rich in TDs. If such particles are immersed in LCs, they could enforce additional TDs in the surrounding [21] LC medium if they impose sufficiently strong anchoring. Such defects can mediate the elastic forces among colloidal particles, which could be exploited as a self-assembling mechanism in which complex hierarchical superstructures could form by judicious selection of LC, confining geometries and/or boundary conditions, and shapes of colloidal particles [140,149]. One could also form diverse configurations by immersing LC shells [150-154] (i.e. thin LC films covering colloids) within an isotropic fluid. Due to their curvature [155,156], TDs are inevitably formed for nontoroidal topologies of colloids. (They also might be formed for toroidal geometries if strong enough local curvatures are present [157]). Nelson [150] proposed that such systems could be exploited for scaled soft crystals with a characteristic lattice size in the micometer regime, where the topological defects within shells play the role of atomic valence of real crystals. It was suggested that by changing number and spatial position of TDs within LC shells, one

could create programmable crystal structures that could exhibit symmetries not encountered in solid “real”-atom based crystals. And of course, different symmetries open the door to different functionalities.

The resulting complex tunable systems enable diverse application. Examples include optical applications [158,159], switchable 2D diffraction gratings and tunable lens [25], haptic displays [160], smart windows [161], sensitive detectors [12], artificial muscles [162], soft robotics [163], substrates for flexible devices in aerospace, medicine, or consumer goods [74], actuators [164], flexible electronics [165], energy storage devices (e.g. batteries, supercapacitors) [166], and solar harvesting [167].

In addition, investigations of the dynamic and static behaviours of disclinations might deepen our basic understanding of natural phenomena. Coarsening dynamics of defects in fast-enough quenches yields some insight into the behaviour of the early universe, where disclinations roughly mimic cosmic strings [2]. Chargeless disclination are reminiscent to the intriguing Majorana particles [168], which can simultaneously act as *particles* and *antiparticles*. We remark that these particles could represent neutrinos, whose intriguing behaviour is not understood. Furthermore, it seems that physical fields represent fundamental entities of nature [169]. Consequently, topological defect localized excitations might represent “fundamental particles” in the Standard Model parlance. In fact, Skyrme [170] was the first proposer of this phenomenon. LCs represent an ideal platform in which Skyrmions [171] and related topological excitations could be experimentally studied relatively easily. Consequently, several issues could be analysed in detail, thus deepening our understanding of several open problems in physics.

Acknowledgments

A.J.F., B.S.M., A.L.S., and C.R. were supported financially by the U.S. National Science Foundation under Grant DMR1901797 and by the National Aeronautics and Space Administration under grant NNX17AC76G. G.C. acknowledges financial support of the Grant CZ.02.2.69/0.0/0.0/16_027/0008465 for Mobility of Researchers under the Operation Programme Research, Development and Education. G.C., B.R. and Z.K acknowledge financial support of the Grant P1-0125 of the Slovenian Research Agency. B. R. acknowledges the financial support by the Fulbright grant. B. R. and Z. K. acknowledge the financial support of the Grant J1-9147 of the Slovenian Research Agency. S.K acknowledges financial support of the Grants P1–0099 and J1-2457of the Slovenian Research Agency.

The authors declare no competing financial interests.

[1] Mermin N. The Topological Theory of Defects in Ordered Media. Rev Mod Phys. 1979;51:591–648.

[2] Kibble TWB. Topology of cosmic domains and strings. J Phys A: Math. Gen. 1976;9(8):1387–1398.

[3] Zurek WH. Cosmological experiments in superfluid helium? Nature. 1985; 317:505–508.

[4] Kleman M, Lavrentovich OD. Soft Matter Physics: An Introduction. New York (NY): Springer Science & Business Media; 2004.

[5] Volovik GE and Lavrentovich OD. Topological dynamics of defects: boojums in nematic drops. Sov Phys JETP. 1983;58(6):1159–1166.

[6] De Gennes PG and Prost J. The Physics of Liquid Crystals. Oxford: Clarendon; 1994.

[7] Palffy-Muhoray P. The diverse world of liquid crystals. Phys Today. 2007;6(9):54–60.

[8] Lavrentovich OD. Topological defects in dispersed liquid crystals, or words and worlds around liquid crystal drops. Liq Cryst. 1998;24(1):117–126.

[9] Meiboom S, Sethna JP, Anderson PW, et al. Theory of the blue phase of cholesteric liquid crystals. Phys Rev Lett. 1981;46:1216-1219.

[10] Wright DC, Mermin N. Crystalline liquids: the blue phase. Rev Mod Phys. 1989;61:385–432.

[11] Lin IH, Miller DS, Bertics PJ, et al. Endotoxin-induced structural transformations in liquid crystalline droplets. Science. 2011;332:1297–1300.

[12] Lowe AM, Abbott NM. Liquid crystalline for biological applications. Chem Mater. 2012;24(5):746–758.

[13] Guo D, Chen CW, Li CC, et al. Reconfiguration of three-dimensional liquid crystalline photonic crystals by electrostriction. Nat Mater. 2020;19:94–101.

[14] Coursault D, Grand J, Zappone B, et al. Linear Self-Assembly of Nanoparticles Within Liquid Crystal Defect Arrays. Adv Mater. 2012;24:1461–1465.

[15] Dubtsov AV, Pasechnik SV, Shmeliova DV, et al. Light and phospholipid driven structural transitions in nematic microdroplets. App Phys Lett. 2014;105:151606.

[16] Klemenčič E, Trček M, Kutnjak Z, et al. Giant electrocaloric response in smectic liquid crystals with direct smectic-isotropic transition. Sci Rep. 2019;9:1721.

[17] Kikuchi H, Yokota M, Hisakado YH, et al. Polymer-stabilized liquid-crystals blue phases. Nat Mater. 2002;1:64–68.

[18] Karatairi E, Rožič B, Kutnjak Z, et al. Nanoparticle-induced widening of the temperature range of liquid-crystalline blue phases. Phys Rev E. 2010;81:041703.

[19] Wang X, Kim Y, Bukusoglu E, et al. Experimental Insights into the Nanostructure of the Cores of Topological Defects in Liquid Crystals. Phys Rev Lett. 2016;116:147801.

[20] Wang X, Miller DS, Bukusoglu E, et al. Topological Defects in Liquid Crystals as Templates for Molecular Self-assembly. Nat Mater. 2016;15:106–112.

[21] Poulin P, Stark H, Lubensky TC, et al. Novel colloidal interactions in anisotropic fluids. Science. 1997;275:1770–1773.

[22] Pires D, Fleury JB and Galerne Y. Colloid particles in the interaction field of a disclination line in a nematic phase. Phys Rev Lett. 2007; 98:247801.

[23] Tkalec U, Ravnik M, Čopar S, et al. Reconfigurable knots and links in chiral nematic colloids. Science 2011;333:62–65.

[24] Harth K, Stannarius R. Topological Point Defects of Liquid Crystals in Quasi-Two-Dimensional Geometries. Front. in Phys. 2020;8:112–131.

[25] Shin MJ, Yoon DK. Role of Stimuli on Liquid Crystalline Defects: From Defect Engineering to Switchable Functional Materials. Mater. 2020;13:5466–5489.

[26] Kulkarni S, Kumar S, Thareja P. Colloidal and fumed particles in nematic liquid crystals: Self-assembly, confinement and implications on rheology. J Mol Liq. 2021;336:116241.

[27] Stark H. Physics of Colloidal Dispersions in nematic liquid crystals. Phys Rep. 2001;351:387–474.

[28] Lubensky TC, Pettey D, Currier N, et al. Topological defects and interactions in nematic emulsions. Phys Rev E. 1998;57:610–625.

[29] Sanchez T, Chen DTN, DeCamp SJ, et al. Spontaneous motion in hierarchically assembled active matter. Nature. 2012;491:431–434.

[30] Doostmohammadi A, Ignés-Mullol J, Yeomans JM, et al. Active Nematics. Nat. Commun. 2018;9:3246–3259.

[31] Kralj S, Rosso R, Virga EG. Finite-size effects on order reconstruction around nematic defects. Phys Rev E. 2010;81:021702.

[32] Kaiser P, Wiese W, Hess S. Stability and instability of a uniaxial alignment against biaxial distortions in the isotropic and nematic phases of liquid crystals. J Non-Equilib Thermodyn. 1992;17:153–169.

[33] Kralj S and Žumer S. The saddle-splay surface elasticity of nematic structures confined to a cylindrical capillary. Phys Rev E. 1995;51:366–379.

[34] Nobili M and Durand G. Disorientation-induced disordering at a nematic-liquid-crystal–solid interface. Phys Rev A. 1992;46:6174(R).

[35] Virga EG. Variational Theories for Liquid Crystals. Chapman Hall 1994. London.

[36] Nehring J, Saupe A. Calculation of the Elastic Constants of Nematic Liquid Crystals. J Chem Phys. 1972;56:5527–5528.

[37] Rapini A, Papoular M. Distorsion d'une lamelle nematique sous champ magneticue conditions d'ancrage aux Parois [Distortion of a nematic lamella under a magnetic field conditions of anchoring to the Walls]. J. Phys Colloq. 1969;30(C4):54–56.

[38] Selinger JV. Interpretation of saddle-splay and the Oseen-Frank free energy in liquid crystals. Liq Cryst Rev. 2018;6(2):129–142.

[39] Selinger JV. Director deformations, Geometric frustration, and modulated phases in liquid crystals. Soft Condensed Matter (cond-mat.soft). 2021; arXiv:2103.03803.

[40] Machon T and Alexander GP. Umbilic Lines in Orientational Order. Phys Rev X. 2016;6:011033.

[41] Ericksen JL. Inequalities in Liquid Crystal Theory. Phys Fluids. 1966;9:1205–1207.

[42] Gartland EC and Mkaddem S. Instability of radial hedgehog configurations in nematic liquid crystals under Landau–de Gennes free-energy models. Phys Rev E. 1999;59:563–567.

[43] Schopohl N, Sluckin TJ. Defect Core Structure in Nematic Liquid Crystals. Phys Rev Lett. 1987;59:2582–2584.

[44] Kralj S and Virga EG. Universal Fine Structure of Nematic Hedgehogs. J Phys A: Math. Gen. 2001;34:829–838.

[45] Bisi F, Gartland EC, Rosso R, et al. Order Reconstruction in Frustrated Nematic Twist Cells. Phys Rev E. 2003;6:021707.

[46] Mori H and Nakanishi H. On the Stability of Topologically Non-Trivial Point Defects. J Phys Soc Jpn. 1988;57:1281–1286.

[47] Terentjev EM. Disclination loops, standing alone and around solid particles, in nematic liquid crystals. Phys Rev E. 1995;51:1330–1337.

[48] Bradač Z, Kralj S, Svetec M, et al. Annihilation of nematic point defects: Postcollision scenarios. Phys Rev E. 2003;6:050702(R).

[49] Zhou S, Shiyanovskii SV, Park HS, et al. Fine Structure of the Topological Defect Cores Studied for Disclinations in Lyotropic Chromonic Liquid Crystals. Nat Commun. 2017; 8:14974–14981.

[50] Hendry PC, Lawson NS, Lee RAM, et al. Generation of defects in superfluid ^{4}He as an analogue of the formation of cosmic strings. Nature. 1994;368:315–317.

[51] Dodd ME, Hendry PC, Lawson NS, et al. Nonappearance of Vortices in Fast Mechanical Expansions of Liquid ^{4}He through the Lambda Transition. Phys Rev Lett. 1998;81:3703–3706.

[52] Kavoussanaki E, Monaco R, and Rivers RJ. Testing the Kibble-Zurek Scenario with Annular Josephson Tunnel Junctions. Phys Rev Lett. 2000;85:3452–3455.

[53] Digal S, Ray R and Srivastava AM. Observing Correlated Production of Defects and Antidefects in Liquid Crystals. Phys Rev Lett. 1999;83:5030–5033.

[54] Chuang I, Yurke B, Pargellis A, et al. Coarsening dynamics in uniaxial liquid crystals. Phys Rev E. 1993;47:3343–3356.

[55] Chuang I, Durrer R, Turok N, et al. Cosmology in the Laboratory: Defect Dynamics in Liquid Crystals. Science. 1991; 251: 1336–1342.

[56] Bradač Z, Kralj S, Žumer S. Early stage domain coarsening of the isotropic-nematic phase transition. J Chem Phys. 2011;135:024506.

[57] Bradač Z, Kralj S, Žumer S. Molecular dynamics study of isotropic-nematic quench. Phys Rev E. 2002;65:021705.

[58] Billeter JL, Smondyrev AM, Loriot GB, et al. Phase-ordering dynamics of the Gay-Berne nematic liquid crystal. Phys Rev E. 1999;60:6831–6840.

[59] Eakin JN, Xie Y, Pelcovits RA, et al. Zero voltage Freedericksz transition in periodically aligned liquid crystals. Appl Phys Lett. 2004;85:1671–1673.

[60] Crawford GP, Eakin JN, Radcliffe RD, et al. Liquid-crystal diffraction gratings using polarization holography alignment techniques. J Appl Phys. 2005;98:123102.

[61] Gorkhali SP. Intensity and Polarization Holography [dissertation]. Providence RI: Brown University; 2007.

[62] Fleury J-B, Pires D, Galerne Y. Self-Connected 3D Architecture of Microwires. Phys Rev Lett. 2009;103:267801.

[63] Ackerman PJ, Qi Z, Smalyukh II. Optical generation of crystalline, quasicrystalline, and arbitrary arrays of torons in confined cholesteric liquid crystals for patterning of optical vortices in laser beams. Phys Rev E. 2013;86:021703.

[64] Ackerman PJ, Qi Z, Lin Y, et al. Laser-directed hierarchical assembly of liquid crystal defects and control of optical phase singularities. Sci Rep. 2012;2:414–422.

[65] Evans JS, Ackerman PJ, Broer DJ, et al. Optical generation, templating, and polymerization of three-dimensional arrays of liquid-crystal defects decorated by plasmonic nanoparticles. Phys Rev E. 2013;87:032503.

[66] Sohn HRO, Liu CD, Voinsecu R, et al. Optically enriched and guided dynamics of active skyrmions. Opt Express. 2020;28(5):6306–6319.

[67] Culbreath C, Glazar N, Yokoyama H. Note: Automated maskless micro-multidomain photoalignment. Rev Sci Instr. 2011;82:126107.

[68] Glazar N, Culbreath C, Li Y, et al. Switchable liquid-crystal phase-shift mask for super-resolution photolithography based on Pancharatnam–Berry phase. Appl Phys Express. 2015;8:116501.

[69] Wang M, Li Y, Yokoyama H. Artificial web of disclination lines in nematic liquid crystals. Nat Commun. 2017;8:388–395.

[70] Gao Y, Jiang M, Chehui P, et al. High-Resolution and High-Throughput Plasmonic Photopatterning of Complex Molecular Orientations in Liquid Crystal. Adv Mater. 2016;28(12):2353–2358.

[71] Yu H, Jiang M, Guo Y, et al. Plasmonic Metasurfaces with High UV–Vis Transmittance for Photopatterning of Designer Molecular Orientations. Adv Opt Mater. 2019;7(11):1900117.

[72] Guo Y, Jiang M, Afghah S, et al. Photopatterned Designer Disclination Networks in Nematic Liquid Crystals. Adv Opt Mater. 2021;9(16):2100181.

[73] Peng C, Guo Y, Turiv T, et al. Patterning of Lyotropic Chromonic Liquid Crystals by Photoalignment with Photonic Metamasks. Adv Mater. 2017;29:1606112.

[74] Ware TH, McConney ME, Jeong JW, et al. Voxelated liquid crystal elastomers. Science. 2015; 347(6225):982–984.

[75] You R, Choi Y-S, Shin MJ, et al. Reconfigurable periodic liquid crystal defect array via modulation of electric field. Adv Mater Techn. 2019;4:1900454.

[76] Kim MS, Serra F. Tunable large-scale regular arrays of topological defects in nematic liquid crystals. RSC Adv. 2018; 8: 35640–35645.

[77] Sasaki Y, Takahashi J, Tokoawa S, et al. A general control strategy to micropattern topological defects in nematic liquid crystals using ionically charged dielectric surface. Adv Mater Interfaces. 2021;8:2100379.

[78] Sasaki Y, Jampani VSR, Tanaka C. Large-scale self-organization of reconfigurable topological defect networks in nematic liquid crystals. Nat Commun. 2016;7:13238.

[79] Cattaneo L, Kos Ž, Savoini M, et al. Electric field generation of Skyrmion-like structures in a nematic liquid crystal. Soft Matter. 2016;6:853–858.

[80] Aya S, Salamon P, Eber N, et al. Reconfigurable large-scale pattern formation driven by topological defect separation in liquid crystals. Adv Mater Interfaces. 2020; 7:2000139.

[81] Missaoui A, Harth K, Salamon P, et al. Annihilation of point defect pairs in freely suspended liquid-crystal films. Phys Rev Res. 2020;2:013080.

[82] Kim MS, Serra F. Tunable Dynamic Topological Defect Pattern Formation in Nematic Liquid Crystals. Adv Opt Mater. 2020;8(1):1900991.

[83] Kim MS, Serra F. Topological Defect Arrays in Nematic Liquid Crystals Assisted by Polymeric Pillar Arrays: Effect of the Geometry of Pillars. Crystals. 2020;10:314–326.

[84] Guo Y, Shahsava H, Davidson ZS, et al. Precise Control of Lyotropic Chromonic Liquid Crystal Alignment through Surface Topography. ACS Appl Mater Interfaces. 2019;11: 36110–36117.

[85] Rüetschi M, Grütter P, Fünfschilling J, et al. Creation of liquid crystal waveguides with scanning force microscopy. Science.1994;265:512–514.

[86] Kim J-H, Yoneya M, Yokoyama H. Tristable nematic liquid-crystal device using micropatterned surface alignment. Nature. 2002;420:159–162.

[87] Wen B, Mahajan MP, Rosenblatt C. Ultrahigh-resolution liquid crystal display with gray scale. Appl Phys Lett. 2000;76:1240–1242.

[88] Wen, B, Petschek RG, Rosenblatt C. Nematic liquid-crystal polarization gratings by modification of surface alignment. Appl Opt. 2002;41:1246–1250.

[89] Berreman DW. Solid Surface Shape and the Alignment of an Adjacent Nematic Liquid Crystal. Phys Rev Lett. 1972;28:1683–1686.

[90] Geary JM, Goodby JW, Kmetz AR, et al. The mechanism of polymer alignment of liquid-crystal materials. J Appl Phys. 1987;62:4100–4108.

[91] Shioda T, Wen B, Rosenblatt C. Step-wise Freedericksz transition in a nematic liquid crystal. J Appl Phys. 2003;94(12):7502–7504.

[92] Carbone G, Rosenblatt C. Polar Anchoring Strength of a Tilted Nematic: Confirmation of the Dual Easy Axis Model. Phys Rev Lett. 2005;94:057802.

[93] Vaughn KE, Sousa M, Kang D, et al. Continuous control of liquid crystal pretilt angle from homeotropic to planar. Appl Phys Lett. 2007;90:194102.

[94] Missaoui A, Rosenblatt C. Unpublished.

[95] Kim D-H, Seo S-S, Park H-G, et al. High Pretilt Angle Effects on Electro-Optical Property of Ion-Beam Irradiated Liquid Crystal Cells on a Blended Polyimide Surface. Ferroelectrics. 2010;396:67–75.

[96] Nehring J, Saupe A. Schlieren texture in nematic and smectic liquid-crystals. J Chem Soc Faraday Trans II. 1972;68(590):1–15.

[97] Murray BS, Pelcovits RA, Rosenblatt C. Creating arbitrary arrays of two-dimensional topological defects. Phys Rev E 2014;90:052501.

[98] Syed IM, Carbone G, Rosenblatt C, et al. Planar degenerate substrate for micro- and nanopatterned nematic liquid-crystal cells. Phys Rev E. 2005;98:034303.

[99] Kralj S, Murray BS, Rosenblatt C. Decomposition of strongly charged topological defects. Phys Rev E. 2017;95:042702.

[100] Murray BS, Kralj S, Rosenblatt. Decomposition vs. escape of topological defects in a nematic liquid crystal. Soft Matter. 2017;13:8442–8450.

[101] Harkai S, Murray BS, Rosenblatt C, et al. Electric field driven reconfigurable multistable topological defect patterns. Phys Rev Research. 2020;2:013176.

[102] Ferris AJ, Afghah S, Selinger RLB, et al. Electric field-induced crossover from 3D to 2D topological defects in a nematic liquid crystal: experimental verification. Soft Matter. 2020;16:642–650.

[103] Susser AL, Harkai S, Kralj S, et al. Transition from escaped to decomposed nematic defects, and vice versa. Soft Matter. 2020;16:4814–4822.

[104] Susser, AL, Kralj S, Rosenblatt C. Co-revolving topological defects in a nematic liquid crystal. Soft Matter. 2021;17:9616–9623.

[105] Ondris-Crawford RJ, Crawford GP, Žumer S, et al. Curvature-induced configuration transition in confined nematic liquid crystals. Phys Rev Lett. 1993;70:194–197.

[106] Cladis PE, Kleman M. Non-singular disclinations of strength S = + 1 in nematics. J Phys France. 1972;33(5-6):591–598.

[107] Chiccoli C, Feruli I, Lavrentovich OD, et al. Topological defects in schlieren textures of biaxial and uniaxial nematics. Phys Rev E. 2002;66:030701.

[108] Carbone G, Lombardo G, Barberi R, et al. Mechanically Induced Biaxial Transition in a Nanoconfined Nematic Liquid Crystal with a Topological Defect. Phys Rev Lett. 2009;103:167801.

[109] Martinot -Lagarde Ph, Dreyfus-Lambez H, Dozov I. Biaxial melting of the nematic order under a strong electric field. Phys Rev E. 2003;67:051710.

[110] Smalyukh II, Pratibha R, Madhusudana NV, et al. Selective imaging of 3D director fields and study of defects in biaxial smectic A liquid crystals. Eur J Phys E. 2005; 16:179–191.

[111] Carr EF. Influence of electric and magnetic fields on dielectric constant and loss of liquid crystal anisaldazine. J Chem Phys. 1963;38:1536–1540.

[112] Carr EF. Influence of electric fields on the molecular alignment in the liquid crystal p-(ansalamino)-phenyl acetate. Mol Cryst Liq Cryst. 1969;7:253–268.

[113] Helfrich W. Conduction-induced alignment of nematic liquid crystals: Basic model and stability considerations. J Chem Phys. 1969;51:4092–4105.

[114] Pomeau Y, Manneville P. Intermittent Transition to Turbulence in Dissipative Dynamical Systems. Comm Math Phys. 1980;74:189–197.

[115] Oswald P, Dequidt A. Lehmann effect in chiral liquid crystals and Langmuir monolayers: an experimental survey. Liq Cryst. 2009;36:1071–1084.

[116] Backer AS, Callan-Jones AC, Pelcovits RA. Nematic cells with defect-patterned alignment layers. Phys Rev E. 2008;77:021701.

[117] Afghah S, Selinger RLB, Selinger JV. Visualising the crossover between 3D and 2D topological defects in nematic liquid crystals. Liq Cryst. 2018;45:2022–2032.

[118] Duzgun A, Selinger J and Saxena A. Comparing skyrmions and merons in chiral liquid crystals and magnets. Phys Rev E. 2018;97:062706.

[119] Ambrožič M, Gudimalla A, Rosenblatt C, et al. Multiple Twisted Chiral Nematic Structures in Cylindrical Confinement. Crystals 2020;10:576–591.

[120] Fukuda J and Žumer S. Quasi-two-dimensional skyrmion lattices in a chiral nematic liquid crystal. Nat Commun. 2011;2:246–251.

[121] Nych A, Fukuda J, Ognysta U, et al. Spontaneous formation and dynamics of half-skyrmions in a chiral liquid-crystal film. Nat Phys. 2017;13:1215–1220.

[122] Vitelli V. and Turner AM. Anomalous coupling between topological defects and curvature. Phys Rev Lett. 2004;93:215301.

[123] Bowick M, Nelson DR, Travesset A. Curvature-induced defect unbinding in toroidal geometries. Phys Rev E. 2004;69:041102.

[124] Selinger RLB, Konya A, Travesset A, et al. Monte Carlo studies of the XY model on two-dimensional curved surfaces. J Phys Chem B. 2011;115:13989–13993.

[125] Mesarec L, Góźdź W, Iglič A, et al. Effective topological charge cancelation mechanism. Sci Rep. 2016;6:1–12.

[126] Mesarec L, Góźdź W, Iglič A, et al. Normal red blood cells' shape stabilized by membrane's in-plane ordering. Sci Rep. 2019;9:1–11.

[127] Etchegoin, P. Blue phases of cholesteric liquid crystals as thermotropic photonic crystals. Phys Rev E. 2000;62:1435–1437.

[128] Cao W, Muñoz A, Palffy-Muhoray P, et al. Lasing in a three-dimensional photonic crystal of the liquid crystal blue phase II. Nat Mat. 2002;1:111–113.

[129] Yoshida H, Tanaka Y, Kawamoto K, et al. Nanoparticle-Stabilized Cholesteric Blue Phases. Appl Phys Express. 2009;2:121501.

[130] Cordoyiannis G, Losada-Pérez P, Tripathi CSP, et al. Blue phase III widening in CE6-dispersed surface-functionalized CdSe nanoparticles. Liq Cryst. 2010; 11:1419–1426.

[131] Dierking I, Blenkhorn W, Credland E, et al. Stabilising liquid crystalline Blue Phases. Soft Matter. 2012;8:4355–4362.

[132] Rožič B, Tzitzios V, Karatairi E, et al. Theoretical and experimental study of the nanoparticle-driven blue phase stabilization. Eur Phys J E. 2011;3:17–28.

[133] Cordoyiannis G, Lavrič M, Trček M, et al. Quantum Dot-Driven Stabilization of Liquid-Crystalline Blue Phases. Front Phys. 2020;8:315–323.

[134] Cordoyiannis G, Jampani VSR, Kralj S, et al. Different modulated structures of topological defects stabilized by adaptive targeting nanoparticles. Soft Matter. 2013;9: 3956–3964.

[135] Lavrič M, Tzitzios V, Kralj S, et al. The effect of graphene on liquid-crystalline blue phases. Appl Phys Lett. 2013;103:143116.

[136] Lavrič M, Cordoyiannis G, Kralj S, et al. Effect of anisotropic MoS_2 nanoparticles on the blue phase range of a chiral liquid crystal. Appl Opt. 2013;52:E47–E52.

[137] Lavrič M, Tzitzios V, Cordoyiannis G, et al. Blue phase range widening induced by laponite nanoplatelets in the chiral liquid crystal CE8. Mol Cryst Liq Cryst. 2015;615:14–18.

[138] Lavrič M, Cordoyiannis G, Tzitzios V, et al. Blue phase stabilization by CoPt-decorated reduced-graphene oxide nanosheets dispersed in a chiral liquid crystal. J Appl Phys. 2020;127: 095101.

[139] Cordoyiannis G, Lavrič M, Tzitzios V, et al. Experimental Advances in Nanoparticle-Driven Stabilization of Liquid-Crystalline Blue Phases and Twist-Grain Boundary Phases. Nanomaterials. 2021;11:2968–19.

[140] Čopar S, Ravnik M and Žumer S. Introduction to Colloidal and Microfluidic Nematic Microstructures. Crystals. 2021;11:956–21.

[141] Pasini P, Chiccoli C and Zannoni C. Liquid crystal lattice models II. Confned systems, in Advances in the Computer Simulations of Liquid Crystals. Pasini P and Zannoni C, editors. Dordrecth: Kluwer. 2000;121–138.

[142] Chiccoli C, Pasini P, Zannoni C, et al. From Point to Filament Defects in Hybrid Nematic Films. Sci Rep. 2019;9:17941.

[143] Svetec M, Kralj S, Bradač Z, et al. Annihilation of nematic point defects: pre-collision and post-collision evolution. Eur Phys J E. 2006;19:71–79.

[144] Lubensky TC, Renn SR. Twist-grain-boundary phases near the nematic–smectic-A–smectic-C point in liquid crystals. Phys Rev A. 1990;41:4392–4401.

[145] Navailles L, Barois P, Nguyen HT. X-ray measurement of the twist grain boundary angle in the liquid crystal analog of the Abrikosov phase. Phys Rev Lett. 1993;71:545–548.

[146] Renn SR, Lubensky TC. Existence of a Sm-C Grain Boundary Phase at the Chiral MAC Point. Mol Cryst Liq Cryst. 1991;209:349–355.

[147] Coursault D, Ibrahim BH, Pelliser L, et al. Modeling the optical properties of self-organized arrays of liquid crystal defects. Opt Express. 2014;22:23182–23191.

[148] Xia Y, Cedillo-Servin G, Kamien RD, et al. Guided Folding of Nematic Liquid Crystal Elastomer Sheets into 3D via Patterned 1D Microchannels. Adv Mater. 2016;28:9637–9643.

[149] Senyuk B, Liu Q, He S, Kamien RD, Kusner RB, Lubensky TC and Smalyukh II. Topological colloids. Nature. 2013;493:200–205.

[150] Nelson DR. Toward a tetravalent chemistry of colloids. Nano Lett. 2002;2:1125-1129.

[151] Vitelli V, Nelson DR. Nematic textures in spherical shells. Phys Rev E. 2006;74(2):021711.

[152] Skačej G, Zannoni C. Controlling surface defect valence in colloids. Phys Rev Lett. 2008; 100(19):197802.

[153] Lopez-Leon T, Koning V, Devaiah KBS, et al. Frustrated nematic order in spherical geometries. Nat Phys. 2011;7(5):391–394.

[154] Mesarec L, Iglič A, Kralj-Iglič V, et al. Curvature Potential Unveiled Topological Defect Attractors. Crystals. 2021;11: 539–555.

[155] Turner AM, Vitelli V and Nelson DR. Vortices on curved surfaces. Rev Mod Phys. 2010;82:1301–1348.

[156] Rosso R, Virga EG, Kralj S. Parallel transport and 57defects on nematic shells. Continuum Mech Thermodyn. 2012;24:643–664.

[157] Jesenek D, Kralj S, Rosso R, et al. Defect unbinding on a toroidal nematic shell. Soft Matter. 2015;11:2434–2444.

[158] Song YM, Xie YZ, Malyarchuk V, et al. Digital cameras with designs inspired by the arthropod eye. Nature. 2013;497:95–99.

[159] Chen L, Li Y, Fan J, et al. Photoresponsive Monodisperse Cholesteric Liquid Crystalline Microshells for Tunable Omnidirectional Lasing Enabled by a Visible Light-Driven Chiral Molecular Switch. Adv Opt Mater. 2014;2:845–849.

[160] Liu D, Broer DJ. Self-assembled dynamic 3D fingerprints in liquid-crystal coatings towards controllable friction and adhesion. Angew Chem Int Ed. 2014;53:4542–4546.

[161] Ge D, Lee E, Yang L, Cho Y, Li M, Gianola DS, Yang S. A robust smart window: reversibly switching from high transparency to angle-independent structural color display. Adv Mater. 2015;27:2489–2495.

[162] Jager EWH, Smela E, Inganas O. Microfabricating conjugated polymer actuators. Science. 2000;290:1540–1545.

[163] Haan de LT, Schenning APHJ, Broer DJ. Programmed morphing of liquid crystal networks. Polymer. 2014;55:5885–5896.

[164] Keplinger C, Sun Y-E, Foo CC, et al. Stretchable, transparent, ionic conductors. Science. 2013;341:984–987.

[165] Kim DH, Lu NS, Ma R, et al. Epidermal electronics. Science. 2011;333:838–843.

[166] Xu S, Zhang YH, Cho J, Lee J, et al. Stretchable batteries with self-similar serpentine interconnects and integrated wireless recharging systems. Nat Commun. 2013;4:1543–1551.

[167] Yin R, Xu W, Kondo M, et al. Can sunlight drive the photoinduced bending of polymer films? J Mater Chem. 2009;19:3141–3143.

[168] Wilczek F. Majorana returns. Nat Phys. 2009;5:614–618.

[169] Hobson A. There are no particles, there are only fields. Am J Phys. 2013;81:211–223.

[170] Skyrme THR. A unified field theory of mesons and baryons. Nucl Phys. 1962; 31:556–569.

[171] Smalyukh II. Review: knots and other new topological effects in liquid crystals and Colloids. Rep Prog Phys. 2020;83:106601.